METHODS OF FITTING COMPRESSIONAL AND SHEAR WAVE VELOCITIES VERSUS SATURATION CURVES AND THE INTERPRETATION OF LABORATORY VELOCITY MEASUREMENTS IN PARTIALLY SATURATED ROCKS

A Thesis

Presented to

the Faculty of the Department of Earth and Atmospheric Sciences

University of Houston

In Partial Fulfillment

of the Requirements for the Degree

Master of Science

By

FIRAS ALJARRAH

December 2009

METHODS OF FITTING COMPRESSIONAL AND SHEAR WAVE VELOCITIES VERSUS SATURATION CURVES AND THE INTERPRETATION OF LABORATORY VELOCITY MEASUREMENTS IN PARTIALLY SATURATED ROCKS

_____

FIRAS ALJARRAH

APPROVED:

_____

Dr. John Castagna, Chairman

_____

Dr.Evgeny M.Chesnokov, Member

_____

Dr. M Amin Kayali, Member

_____

Dean, College of Natural Sciences and
Mathematics

Acknowledgements

My sincere gratitude goes to my adviser Dr. John Castagna for his timely advice and encouragement. I also wish to thank my committee members, Dr. Evgeny M. Chesnokov and Dr. Amin Kayali for their support and advice. I acknowledge all students who provided assistance during this research and the preparation for my defense. I acknowledge all professors whose classes I took, which enabled me to carry out this research. My deepest gratitude goes to my parents for their constant encouragement and great support in my achievement of this goal. I would like to thank my sisters for their unconditional advice and encouragement. I thank all friends and colleagues for their friendship, encouragement, and prayers. For all those whose names I did not mention, it wouldn't have been possible without you all. Finally, I wish to thank God for all I have been given.

METHODS OF FITTING COMPRESSIONAL AND SHEAR WAVE VELOCITIES VERSUS SATURATION CURVES AND THE INTERPRETATION OF LABORATORY VELOCITY MEASUREMENTS IN PARTIALLY SATURATED ROCKS

An Abstract of a Thesis

Presented to

the Faculty of the Department of Earth and Atmospheric Sciences

University of Houston

In Partial Fulfillment

of the Requirements for the Degree

Master of Science

By

FIRAS ALJARRAH

December 2009

Abstract

It is well known that laboratory measurements of P-wave velocity versus saturation do not behave in accordance with Biot-Gassmann equations. There are some missing physical mechanisms (squirt flow dispersion, fluid distribution in different aspect ratio pores…) and also experimental errors in measuring the porosity under environmental conditions. Laboratory P-wave velocity versus saturation curves can be fit using Biot's high frequency equations by: (1) varying the mass coupling factor value in order to compensate for the error in the assumed value, and (2) separating the total porosity into acoustically connected and disconnected portions by applying velocity-porosity empirical relations. The ratio of connected to total porosity representing a free parameter gives the freedom to fit the ending point of the curves and ignores the squirt flow dispersion mechanism. The saturation curves can be interpreted depending on three types of saturation systems: (1) uniform saturation where the gas and water fills the pores of different shapes homogenously at low water saturation, (2) fully segregated saturation where the gas fills the pores of high aspect ratio at high water saturation, and (3) patchy segregation (transitional zone) saturation where the gas exhibits heterogeneous distribution as patches of uniform and fully segregated saturation. Dispersion correction should be considered at sonic logs and lab frequencies. The results can be used to enhance seismic interpretations like bright spots, to maximize the recovery of known hydrocarbon reserves, to apply fluid substitution at a given frequency, and to understand elastic wave velocity at different scales (sonic, seismic).

Table of Contents

Chapter 1   INTRODUCTION

1.1   Introduction

One of the most important matters in rock physics is to predict elastic velocities in rocks saturated with mixed fluids like water-gas and water-oil. Seismic velocities are very significant geophysical tools in reservoir applications. Elastic wave velocities vary with fluid saturation, and the influence of fluid saturation on elastic wave velocities in porous rocks is related to many factors, like pore geometry, fluid phase distribution, compressibility, acoustic coupling factors between solid and liquid, and pressure, temperature, and attenuation mechanisms.

Identifying the effect of mixed fluid saturation like water-gas or oil-gas on elastic velocities is quite important in the interpretation of seismic direct hydrocarbon indicators (DHI) and for time-lapse observation of reservoir production, since the mixed fluids share the porous formations at the top part of gas-capped reservoirs. So it is necessary to know the relationship between fluid saturation and seismic characteristics like elastic moduli, velocity dispersion, and attenuation.

The effects of mixed fluid saturation on elastic velocities of porous media have been considered by both theoretical and experimental techniques. Laboratory measurements are used to explain how water and gas saturation affects acoustic velocities in porous rocks (Gregory, 1976; Domenico, 1977; Murphy, 1984). Theoretically, the variation of the compressional and shear wave velocities with water-gas saturation has been calculated by Domenico (1977), using Biot's theory (1956) and Geertsma (1961) equations. The calculated results are not consistent with laboratory measurements of ultrasonic velocities as a function of water-gas saturation. The inconsistency between the

theoretical model and the measurement model is related to many reasons like dispersion mechanisms and attenuation, fluid phase distribution, effective fluid bulk moduli, and different environmental factors like pressure, temperature, and age.

Fitting the curves of water-gas saturation versus elastic velocities theoretically or empirically helps in using the right model in interpretational applications, like applying fluid substitution modeling at sonic frequencies, correcting for the physical dispersion mechanism (velocity dependent frequency) that could happen in the borehole invasion of the sonic well-logs, enhancing different reservoir models like saturation versus bulk and shear moduli, and using the ultrasonic velocities versus saturation models to understand the behavior of elastic velocities at different frequencies (e.g., sonic, seismic).

1.2   Objectives

The objectives of this thesis are:

- To fit the ultrasonic laboratory compressional (P-wave) and shear (S-wave) velocities versus water-gas saturation curves by using high frequency Biot's equations for different types of sedimentary rocks of different porosities.

- To model and interpret ultrasonic laboratory velocity measurements in partially gas-saturated rocks reported in the literature, and compare them with our physical model in order to compensate for theoretical and experimental errors.

1.3   Layout of thesis

We will talk about some wave propagation theories in porous media. Gassmann's equations will be introduced with some details on calculating elastic moduli parameters. In chapter 3 we will talk about experiments and laboratory measurements, how elastic

wave velocities are measured in the lab, and the techniques in establishing the saturation inside a rock sample. A general idea of attenuation and dispersion in porous media will be presented in chapter 4. Our method of ignoring the squirt flow dispersion mechanism is introduced in chapter 5. Results and interpretations of laboratory data are presented in chapter 6. All the data were taken from the geophysical literature. Conclusions and a discussion will be introduced in chapter 7.

Chapter 2   THEORY

In this chapter we will introduce Gassmann's equations and Biot's relations. We will present some mathematical calculations of elastic moduli and some theoretical interpretations.

2.1   Wave propagation theories in porous media

2.1.1   Gassmann's relations

There are many theories of wave propagation in porous media in the geophysical literature. Gassmann's equation (1951) is used to predict velocities in porous media with mixed fluids like water-gas or water-oil. When the seismic wave passes through a porous saturated rock, the pore pressure tries to resist the compression of the seismic wave. The resistance of the volumetric compression is called the bulk modulus (K). Gassmann's equations calculate the increase in the saturated bulk modulus (K_{sat}) of the rock.

Gassmann's relations relate the porosity (ϕ), the bulk modulus of the mineral matrix (K_o), the bulk modulus of the rock frame (K^*), and the bulk modulus of the pore fluids (K_{fl}) to the saturated bulk modulus of the same rock (K_{sat}). This is shown in Equations (1), (2), and (3):

$$\frac{K_{sat}}{K_o - K_{sat}} = \frac{K^*}{K_o - K^*} + \frac{K_f}{\phi(K_o - K_f)} \qquad ; \qquad (1)$$

$$K_{sat} = K^* + \frac{\left(1 - \dfrac{K^*}{K_o}\right)^2}{\dfrac{\phi}{K_{fl}} + \dfrac{(1-\phi)}{K_o} - \dfrac{K^*}{K_o{}^2}} \qquad ; \text{ and} \qquad (2)$$

$$\mu_{dry} = \mu_{sat} \qquad , \qquad (3)$$

11

where K^* = effective bulk modulus of porous rock frame or skeleton,

K_{sat} = effective bulk modulus of the rock with pore fluid,

K_o = bulk modulus of mineral (grains),

K_{fl} = effective bulk modulus of pore fluid,

ϕ = porosity,

μ^* = effective shear modulus of rock skeleton, and

μ_{sat} = effective shear modulus of rock with pore fluid.

Equations (1) and (2) are the same but in different algebraic order.

2.1.1.1 Gassmann's assumptions

Assumption (1): Gassmann's equations are valid only at low frequencies less than few hundred Hertz (long wavelength). Physically this means there is enough time for the pore pressure to equilibrate through the pore space. The length range of pressure equilibrium is larger than the pore sizes and less than the wavelength (λ) of the seismic wave. So for high frequencies like ultrasonic frequencies (1 MHz), Gassmann's equations are not applicable, and therefore we should use Biot's high frequency equations (1956). Assumption (2): Gassmann's theory assumes that the rock is isotropic and homogeneous; physically this means the rock has the same physical properties in all directions. However, Brown and Korringa (1975) extended Gassmann's relations to include anisotropy properties. Assumption (3): all pores are communicating, which means the rock has a high connected porosity, and there are no isolated pores in the rock. This assumption refers to the full relaxation situation of the pore fluid when the wave passes through the rock. The connected pores are in relation to the wave frequency. Because of

the first assumption that includes an infinite wavelength (zero frequency), most rocks can match this assumption, especially unconsolidated rocks with high porosity and permeability. Velocities measured at high frequencies, like sonic logs and laboratory measurements usually are higher than those calculated with Gassmann's equations. Assumption (4): there are no chemical or physical reactions between solids and fluids, and pore fluid is coupled strongly to the frame of the rock. In fact, rocks saturated with fluids soften or harden the rock frame. Assumption (5): the rock system is closed; there is no fluid flow in or out of the surface of the rock. Assumption (6): the fluids that fill the pores have zero viscosity. Like Assumption (3), this is in relation to the wavelength in order to emphasize that pressure equilibrium of pore fluid will be complete. High viscosity fluids are not easy to equilibrate. In fact, most fluids have finite viscosity; and most waves have finite wavelengths. There is a big difference in bulk and shear moduli between fluids and solids, and for the previous reasons a relative motion between fluids and solids will occur; therefore, waves are dispersive. This is one of the reasons why laboratory velocity measurements are higher than those calculated with Gassmann's equations at high water saturation.

Gassmann's theory also considers that the shear modulus is not affected by pore fluid, and there is no assumption for the pore geometry. However, the Kuster-Toksoz (1974) theory considers the shape, size, and distribution of cracks in the rock.

2.1.1.2 Using Gassmann's equations

In isotropic rock, the bulk modulus (K) or incompressibility is defined as the ratio of hydrostatic stress to volumetric strain. Shear modulus (μ) is defined as the ratio of shear stress to shear strain.

Gassmann's equations can calculate the effective bulk moduli of saturated rock from the dry frame (skeleton) moduli and vice versa. Usually the bulk modulus of rock skeleton is unknown, but we can calculate the bulk modulus of the fluid saturated rock (K_{sat}) if we know the compressional-wave velocity (V_P), the shear-wave velocity (V_S), and the bulk density (ρ_b) of the total rock at full water saturation from the following equations:

$$V_P = \sqrt{\frac{K_{sat} + 4/3\mu_{sat}}{\rho_b}} \quad , \tag{4}$$

$$K_{sat} = \rho_b (V_P - \frac{4}{3}\mu_{sat}) \quad , \tag{5}$$

$$V_S = \sqrt{\frac{\mu_{sat}}{\rho_b}} \quad , \tag{6}$$

$$\mu_{sat} = V_S^2 \rho_b \quad , \text{and} \tag{7}$$

$$\rho_b = \rho_{ma}(1-\phi) + \rho_f\phi \quad , \tag{8}$$

where ρ_{ma} = density of rock matrix (grains),

ρ_{fl} = density of the pore fluid, and

ϕ = porosity, which is the ratio of pore space to the total volume of the rock.

The density of pore fluid is related to water saturation and to the density of the different mixed fluids in the rock by the following equation:

$$\rho_{fl} = \rho_{HYD}(1-S_w) + \rho_{BR}S_w \tag{9}$$

where ρ_{HYD} = density of hydrocarbons,

ρ_{BR} = density of brine, and

S_w =   water saturation.

Gassmann's equations have many parameters to calculate the effect of fluids on seismic velocities. Usually laboratory measurements help to estimate the bulk and shear moduli of the rock frame, grain density, porosity, and fluid bulk modulus. When the lab data are not available, we should use well log data, for example, estimating the porosity from neutron or sonic logs. Or, we can use empirical equations and effective media theories, since most rocks consist of more than two materials.

2.1.1.3.   Estimating (K_{matrix}) Voigt, Reuss, and Hill moduli models

We can calculate the effective bulk modulus of a mineral matrix using the application of Voigt-Reuss-Hill (Mavko 1998). Three things should be known: the porosity, the bulk moduli of the different phases, and the volumetric percentage of every individual mineral. The medium is assumed to be isotropic, linear, and elastic.

Voigt (1928) proposed the stiff upper bound of the effective elastic moduli. The upper bound describes an isostrain situation, because the strain is equal on all the layers, but the stress is different, as shown in Figure (1a).

(a) Isostrain situation (Voigt)   (b) Isostress situation (Reuss)
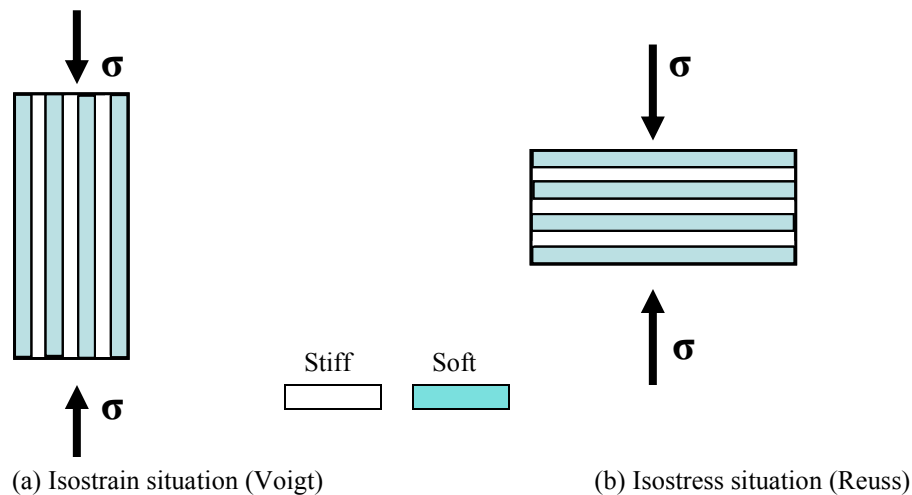
Figure (1): Sketch showing the stress-strain situation in effective media.

15

The Voigt effective bulk modulus can be calculated from the following relation:

$$K_{matrix,Voigt} = \sum_{i=1}^{n} F_i K_i \quad , \tag{10}$$

where F_i = the volumetric fraction of the ith component, and

K_i = the elastic bulk modules of the ith component.

Voigt's upper bound is used to calculate fluid and matrix properties of a linear mix of materials.

Reuss (1929) proposed the soft lower bound of the effective elastic moduli. The lower bound describes the isostress situation, because Reuss assumed that stress applied on materials is the same, but strain is different. Every layer shows a different deformation as shown in Figure (1b). The Reuss effective bulk modulus can be calculated from the following relation:

$$K_{matrix,Reuss} = \left(\sum_{i=1}^{n} \frac{F_i}{K_i} \right)^{-1} \quad , \tag{11}$$

where F_i = the volumetric fraction of the ith component, and

K_i = the elastic bulk modules of the ith component.

Reuss' lower bound is used to calculate the fluid and matrix properties of a harmonic mix of materials. Reuss' lower bound describes the effective moduli situation of mixed materials of solids and fluids like gas and water.

Hill (1952) proposed his bound by taking the average between Voigt and Reuss in order to get a better estimation of the effective bulk modulus of the rock matrix.

2.1.1.4   Estimating (K_{fluid})-Wood's pore fluid modulus model

Wood's equation (1955) can estimate the effective bulk modulus of the pore fluid (K_{fluid}). Wood's equation relates the velocity to the pore fluid bulk modulus assuming zero shear modulus using Equation (12). Wood used the Reuss fluid compressibility average to calculate the effective pore fluid bulk modulus using Equation (13), and (14):

$$V_P = \sqrt{\frac{K_{fluid,Reuss}}{\rho_{sat}}} \qquad , \qquad (12)$$

where V_P = compressional wave velocity,

$K_{fluid,Reuss}$ = Ruess fluid compressibility average, and

ρ_{sat} = saturated rock bulk density.

$$K_{fluid,Reuss} = \left(\frac{(1-\phi)}{K_{Matrix}} + \frac{(S_w)(\phi)}{K_{Water}} + \frac{(1-S_w)(\phi)}{K_{HYD}} \right)^{-1} \qquad , \qquad (13)$$

where K_{Matrix} = bulk modulus of the rock minerals,

K_{Water} = bulk modulus of water under reservoir conditions,

K_{HYD} = bulk modulus of hydrocarbon under reservoir conditions,

ϕ = porosity, and

S_w = water saturation.

$$\rho_{sat} = \rho_{ma}(1-\phi) + \rho_w S_w \phi + \rho_{hc}(1-S_w)\phi \qquad , \qquad (14)$$

where ρ_{ma} = density of the rock minerals,

ρ_w = density of water under reservoir conditions, and

ρ_{hc} = density of hydrocarbon under reservoir conditions.

Gassmann's relation assumes that the pores are connected, and refers that the fluid is uniformly distributed, so the Reuss average is more applicable to calculate the effective fluid bulk modulus through the following equation:

$$K_{fluid} = \left(\frac{S_w}{K_w} + \frac{1-S_w}{K_{gas}} \right)^{-1} \qquad . \tag{15}$$

If the fluid distribution in not uniform, then we use the Wood-Voigt equation to calculate the stiffer effective bulk modulus of pore fluid from the following equation:

$$K_{fluid,Voigt} = (1-\phi)K_{Matrix} + (S_w)(\phi)K_{Water} + (1-S_w)(\phi)K_{HYD} \qquad . \tag{16}$$

2.1.1.5. Estimating (K^*_{frame})

Usually the bulk modulus of the skeleton is unknown; there are many empirical equations to estimate frame bulk modulus. Frame moduli are different from the dry moduli. A frame modulus is the modulus measured at an irreducible amount of water saturation, so the wetting fluid is considered to be part of the rock's frame.

In Gassmann's equation the wetting frame bulk moduli should be used; otherwise, the dry moduli will give very high velocities. So if the saturated bulk modulus is known from Equation (4), based on the measured velocities, we can calculate the frame bulk modulus from Equation (17):

$$K^* = \frac{K_{sat}\left[\dfrac{\phi K_o}{K_{fl}} + 1 - \phi \right] - K_o}{\dfrac{\phi K_o}{K_{fl}} + \dfrac{K_{sat}}{K_o} - 1 - \phi} \qquad , \tag{17}$$

Where $K^* = $ effective bulk modulus of porous rock frame or skeleton,

$K_{sat} = $ effective bulk modulus of the rock with pore fluid,

$K_o = $ bulk modulus of mineral (grains),

18

K_{fl} = effective bulk modulus of pore fluid, and

ϕ = porosity.

The dry bulk modulus is related to the matrix bulk modulus through Biot's coefficient (B), which has values which depend on the porosity of the rock. If the rock is consolidated, the value of B is zero. If the rock is unconsolidated, the value of B is 1. So the range varies from zero to one. The porosity and the bulk modulus of grains should be known. One of the most common experimental methods has been to approximate B as a function of porosity Equations (18), (19), (20), and (21).

$$K_{frame} = (1-B)K_{matrix} \tag{18}$$

$$B = (1 - \frac{K_{frame}}{K_{marrix}}) \tag{19}$$

When $\phi = 0$ $K_{frame} = K_{matrix}$

When $\phi = 1$ $K_{frame} = 0$

$$0 \le \frac{K_{frame}}{K_{matrix}} < 1 \tag{20}$$

$$0 < B \le 1 \tag{21}$$

There are many equations to estimate Biot's coefficient B, like those found in Geertsma (1961), Krief (1990), Nur *et al*. (1991), and Mavko *et al*. (1998).

The dry bulk modulus (K^*) also can be estimated by using the Greenberg-Castagna (1992) inversion of Gassmann's equation:

$$K_{frame} = bK_{matrix} \qquad , \tag{22}$$

$$b = \frac{(XY-1)}{(X+Y-2)} \qquad , \tag{23}$$

$$Y = 1 + \phi(\frac{K_{matrix}}{K_{fluid}} - 1) \quad , \text{and} \tag{24}$$

$$X = \frac{K_{sat}}{K_{matrix}} \quad . \tag{25}$$

Another method to calculate K^* is to use Poisson's ratio of the dry rock when the compressional and shear velocities are known. Solutions were provided by Gregory (1977). When the frame bulk modulus is calculated, it is possible to calculate the other moduli of the rock saturated with mixed fluids. As mentioned before, Gassmann's equations are applicable only at low frequencies.

Gassmann's equations assume that fluid is distributed homogeneously, but Gassmann's relations give unrealistic results of the heterogeneous distribution of mixed fluids (Domenico, 1977). The calculated velocities in partially saturated rocks using Gassmann's equation agree with low frequency data. Murphy (1982) proved that Gassmann's equations agree with the laboratory measurements at low frequencies. On the other hand, Gassmann's equations do not match the high frequency laboratory velocity measurements of Gregory (1976) and Domenico (1976). So for ultrasonic and sonic velocities, Biot-Geertsma equations should be used to estimate velocities in partially saturated rocks.

2.1.2 Biot-Geertsma relations

Biot (1956) developed a wave propagation theory for porous media. Biot assumed that the rock is isotropic, the wavelength of the passing wave is much larger than the pore size, and the grains of the rock have the same bulk and shear moduli. Biot's theory describes the relationship between the fluid phase and the solid (grains) of the rock by

taking into account the motion of the fluid and its viscosity. Also Biot considered all frequency ranges, from the zero frequency limits which are equal to the Gassmann equation limits, to the high frequency limits (infinite) which are relevant to ultrasonic laboratory measurements. Geertsma and Smit (1961) expressed Biot's equations through mathematical expressions that relate the compressional and shear velocity to its wavelength (frequency) at both zero frequency and infinite frequency. For zero frequency the compressional and shear wave velocities are given by:

$$V_p = \left\{ \frac{1}{\rho_b} \left[\left(\frac{\beta}{C_s} + \frac{4}{3}\mu \right) + \frac{(1-\beta)^2}{(1-\phi-\beta)C_s + \phi C_f} \right] \right\}^{1/2} \quad \text{and} \tag{26}$$

$$V_s = \left[\frac{\mu}{\rho_b} \right]^{1/2} , \tag{27}$$

where C_b = compressibility of the rock frame,

   C_s = compressibility of the solid minerals,

   C_f = compressibility of the pore fluid,

   ρ_b = rock total bulk density,

   ρ_f = density of the pore fluid,

   ϕ = porosity,

   μ = shear modulus of the rock frame, and

   β = the ratio C_s / C_b.

For infinite frequency the compressional and shear wave velocities are given by Equations (28), and (29).

$$V_P = \left\{ \left[\left(\frac{1}{C_b} + \frac{4}{3}\mu \right) + \frac{\frac{\phi\rho_b}{\kappa\rho_f} + (1-\beta)(1-\beta-2\phi/\kappa)}{(1-\phi-\beta)C_s + \phi C_f} \right] \cdot \frac{1}{\rho_b\left(1 - \frac{\rho_f\phi}{\rho_b\kappa}\right)} \right\}^{\frac{1}{2}} \quad ; \quad (28)$$

$$V_s = \left(\frac{\mu}{\rho_b(1 - \frac{\rho_f\phi}{\rho_b\kappa})} \right)^{\frac{1}{2}} \quad , \quad (29)$$

where C_b = compressibility of the rock frame,

C_s = compressibility of the solid minerals,

C_f = compressibility of the pore fluid,

ρ_b = rock total bulk density,

ρ_f = density of the pore fluid,

ϕ = porosity,

μ = shear modulus of the rock frame,

β = ratio C_s / C_b, and

κ = mass coupling factor between the fluid and solid.

The difference between the zero frequency equations (26, 27) and the infinite frequency equations (28, 29) is the mass coupling factor (κ), which has values from one ($\kappa=1$), which means no coupling between fluid and solid, to infinite ($\kappa = \infty$), which means a perfect coupling between fluids and solids.

The situation at the complete mass coupling factor gives the zero frequency Equations (26) and (27); they are equal to Gassmann' relations:

$$C_f = S_w C_w + (1 - S_w) C_g \qquad , \tag{30}$$

where C_f = fluid compressibility,

C_w = compressibility of water,

C_g = compressibility of gas, and

S_w = water saturation.

Equation (30) represents the fluid compressibility as the fluid distributed homogenously, which is the Ruess average. If the fluid distribution is segregated, then the inverse of Equation (30) should be used which, is the Voigt average:

$$C_f = \left(\frac{S_w}{C_w} + \frac{(1 - S_w)}{C_g} \right)^{-1} \qquad . \tag{31}$$

2.2 Previous theoretical interpretations

The changing in elastic wave velocities with fluid saturation was calculated theoretically by Domenico (1974) using Biot (1956) and Geertsma (1961). The shape of the resulting model is shown in Figure (2).

Theoretically, the total shear modulus (μ_{sat}) is assumed to be independent of saturation and equal to the dry shear modulus (μ_{Dry}).
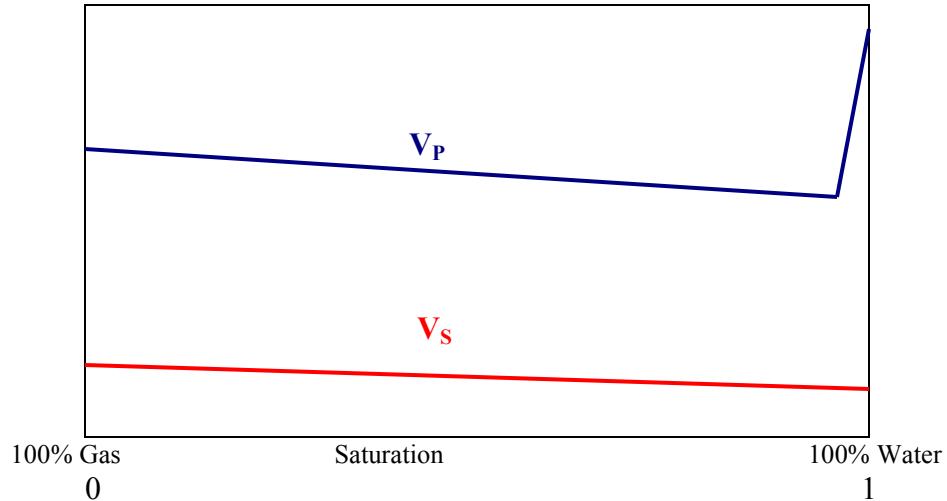
Figure (2): Changing of compressional and shear velocities with water saturation as calculated theoretically by Domenico (1974).

There is a nonlinear increase in compressional wave velocity with water saturation. Starting from zero-water saturation or full-gas saturation, compressional wave velocity decreases with increasing water saturation because density increases; from Equation (4), velocity is inversely proportional to bulk density. At very high water saturation the fluid bulk modulus controls the effect in changing the value of compressional velocity more than bulk density.

The value of compressional wave velocity increases strongly until it reaches full-water saturation, also known from Equation (4); the saturated bulk modulus is proportional to the compressional wave velocity. When the fluid bulk modulus increases, the saturated bulk modulus increases, and results in increasing the compressional wave velocity. The shear velocity decreases linearly with water saturation because the bulk density increases; from Equation (6), bulk density is inversely proportional to shear velocity.

Chapter 3 EXPERIMENTS AND LABORATORY MEASUREMENTS

In this chapter we will introduce a general idea about the laboratory measurements reported in the literature. Also we will talk about some measurement techniques in establishing the fluid saturation, and some fluid distribution models.

3.1   Laboratory velocity measurement techniques

Measuring wave propagation velocities in partially saturated rocks depends on some important physical parameters and mechanisms like wave frequency, velocity dispersion, viscosity, wave attenuation, and density.

The wavelength scale varies between different scale measurements. For example, in seismic measurements the frequency scale is less than 200 Hertz; for sonic log measurements the scale is around 10 - 50 Kilohertz = 10^{4} – 50^{4} Hertz; for ultrasonic laboratory measurements the scale is around 1 Megahertz = 10^{6} Hertz. The majority of laboratory methods that measure elastic velocities use some kind of electromechanical transducers for transmitting and receiving elastic waves.

 Figure 3 shows the interactions between a transducer and elastic waves. Velocities are calculated by dividing the length of the rock sample by the recorded travel time of the propagating wave through a rock sample between the transmitting and receiving transducers. The source and the receiver in a transducer consist of crystal materials like quartz or ceramic materials like titanate or zirconate titanate. The frequencies are controlled by the size of the rock sample and the size of the mineral grains. Most ultrasonic velocity measurements use frequencies from 0.2 to 1 MHz. The first arrival of the recorded signal is measured and then the velocity is calculated. The signals are created by the broadband high-voltage electrical pulses. The velocity

measurements were described in detail by (Gregory, 1967, 1976, 1977; Domenico, 1967, 1977).

Motor   Generator

Electrical

Impulse

Mechanical motion communicated
to
Medium of propagation

Electrical

Response

Crystal deformed by electrical field;
Crystal dimensions change

Crystal deformed mechanically;
deformation causes electric field

ELECTROMECHANICAL TRANSDUCER

P-Wave   S-Wave

Direction of Propagation

Not Polarized   Plan Polarized
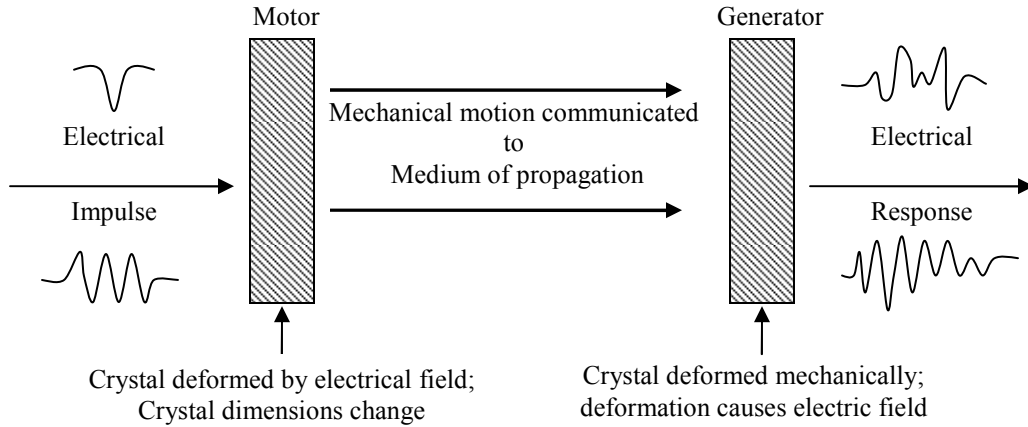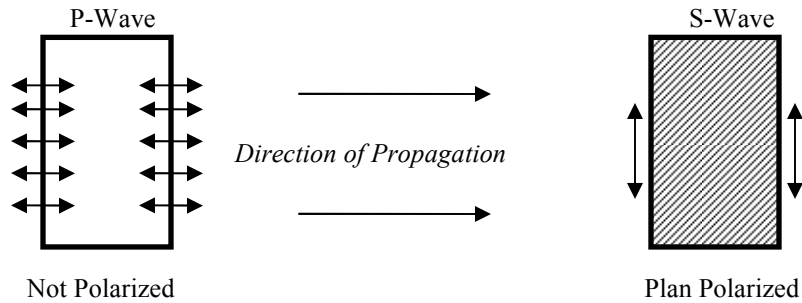
PARTICLE MOTION OF COMPRESSIONAL AND SHEAR WAVES

Figure (3): The action of a transducer and the particle motion of elastic waves.

Figure 4 presents a general diagram of electronic devices used in measuring ultrasonic compressional and shear wave velocities. Four crystal transducers are connected to the rock for passing on and receiving the elastic waves. Two transducers are for compressional waves, and the other two are for shear waves. The switches control both compressional and shear transducers. The pulse and time signal generator creates an

electrical pulse that has a width which varies from 2 to almost 10 μsec. The passing

signal is enlarged by the power amplifier and then displayed on the oscilloscope.

Taken from Domenico, 1976
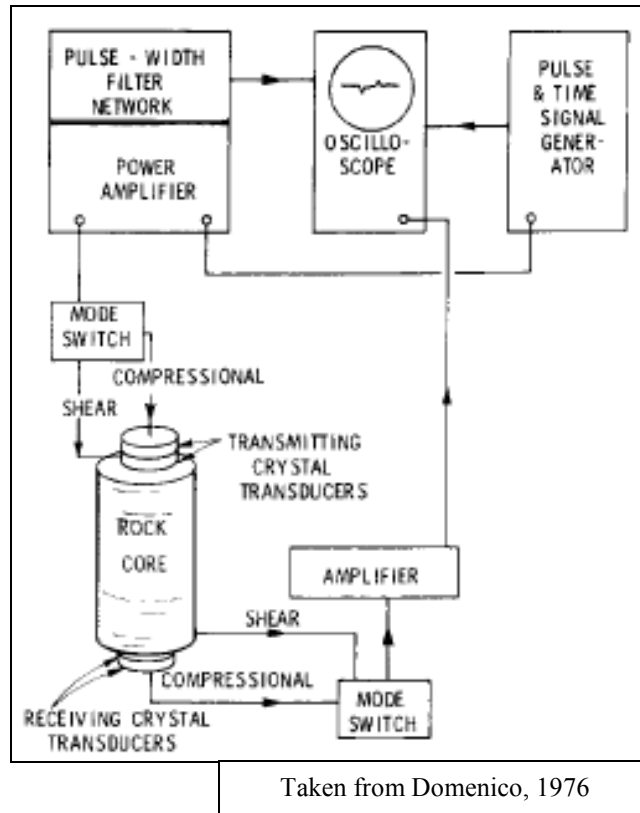
Figure (4): Diagram of electronic tools used in measuring ultrasonic elastic wave traveltime.

Figure 5 shows the timing pulses of both compressional wave and shear wave as

displayed on the oscilloscope. The traveltime of both compressional waves (ΔT_P) and

shear waves (ΔT_S) is the difference in time of the wave passing between the transmitting

and receiving transducers.

TIMING PULSES
DRIVING PULSE

SHEAR WAVE

COMPRESSIONAL
WAVE
TIMING PULSES

Taken from Domenico, 1976
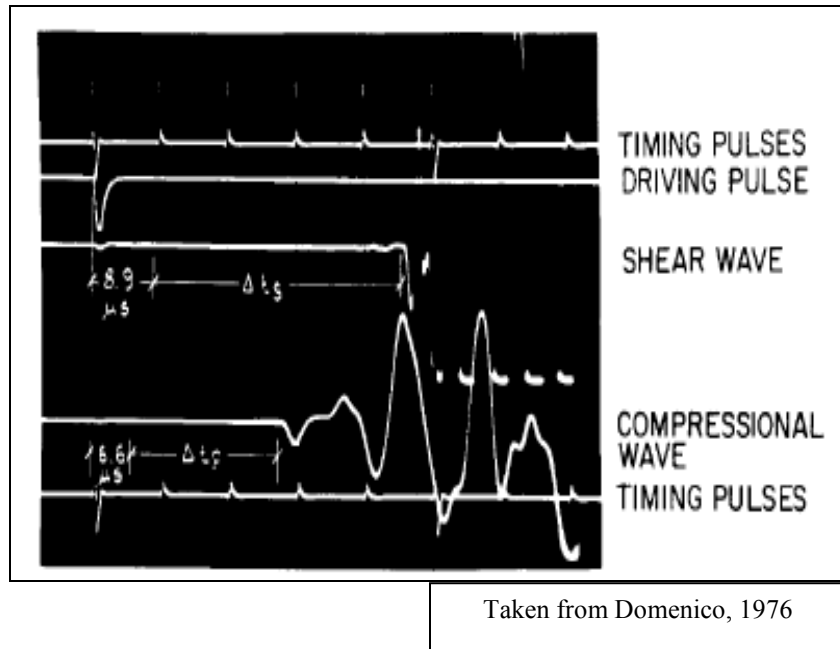
Figure (5): Traveltimes as displayed on Oscilloscope.

Figure 6 shows a general idea about the tool used for sample loading and injecting fluids under different pressure values that could reach 5000 psi, which is equal to the same amount of pressure at a 10,000 foot depth. The pore fluid is injected through a valve, and the pore pressure is controlled by a regulated constant displacement pump.

There are many techniques for controlling the fluid saturation from full-water saturation to full-gas saturation. Generally, full-water saturation is obtained by using the imbibition technique, which is the displacement of air by water, where as full-gas saturation is obtained by using the drainage technique, which is the displacement of water by air by evaporating the water. The distribution and size of injected fluid into a rock sample can be determined by X-ray absorption method. This experimental method was described by Domenico (1976), and Gregory (1977). In general, velocities are measured at various pressure values, and at room temperature (25°).

Taken from Domenico, 1976
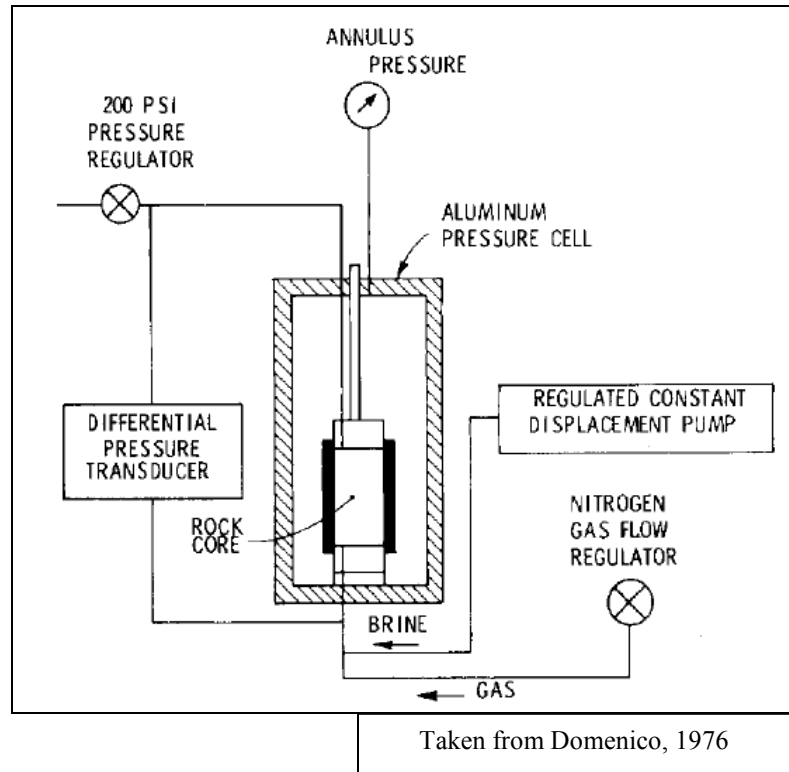
Figure (6): Equipment for injecting the water and gas fluid into the rock sample.

3.2   Previous experimental and theoretical interpretations

Many laboratory experiment results have been published in the geophysical literature (Gregory, 1976, 1977; Domenico, 1976, 1977; Murphy, 1984; Knight and Nolen-Hoeksema, 1990). The experimental results are used to estimate the influence of gas and water saturation on direct hydrocarbon indicators in stacked seismic data like bright spots, since a small amount of gas reduces the velocity and strongly increases the reflection coefficient. Laboratory studies explained the variation of elastic physical properties with fluid saturation, and some measured results from Wyllie (1956) and Murphy (1982) are similar to the theoretical results of Domenico (1974) shown in Figure 2.

29

On the other hand, many laboratory velocity measurements exhibit higher values with increasing water saturation than those calculated theoretically by Biot-Gassmann relations. Some of these laboratory results were obtained by Wyllie *et al*, 1956; Domenico, 1976, 1977; Gregory, 1976, 1977; Knight and Nolen- Hoeksema, 1990.

3.2.1 Interpreting the effect of microscopic fluid distribution

Domenico (1976, 1977) studied the velocity variation with gas-water saturation in two unconsolidated sand samples. Experimentally the saturation was established by using two different techniques; the flow technique and the imbibition technique. The flow technique depends on injecting mixed fluids of gas and water. The gas and water are mixed together before the injection. At low water saturation, the gas volume is large. Gas fills the low aspect ratio pores like cracks while water fills the high aspect ratio pores like spheres or rounded pores. Figure 7 shows the distribution of gas-water fluid in the flow technique. The pores have different aspect ratios. The gas fills the crack first as the S_w increases, and that is why the model called crack preference.

100% Gas   Increasing water saturation   100% Water
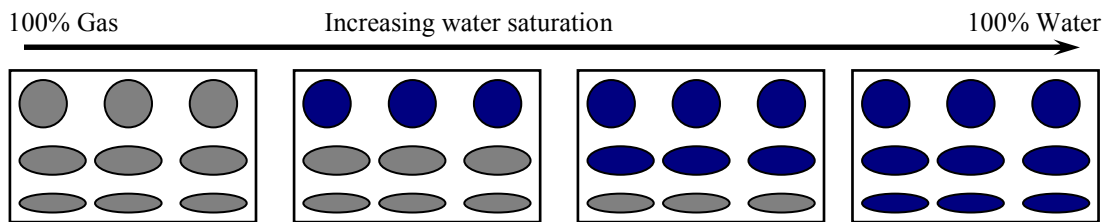
Figure (7): Crack preference distribution model of three different aspect ratio pores, Gas = gray, Water = blue.

The aspect ratio (c=a/b) represents the shape of a single pore seen in (Figure 8). The aspect ratio is defined by the ratio of the length of minor semi axis (a) to the length of the major semi axis (b).
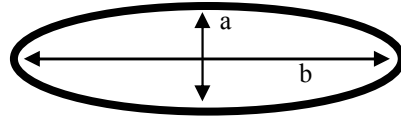
Figure (8): Aspect ratio of a spheroid pore

The distribution of water and gas varies between different pore shapes, because water is considered a wetting fluid with higher viscosity and density than gas, which is a non-wetting fluid. When the amount of gas increases in the mixed fluid before the injection, the water starts to fill the low aspect ratio like cracks, while the gas fluid fills the large pores space; this situation is called the spheroid preference.

Figure 9 shows the distribution of the mixed fluid when the gas has higher volume than the water; and this model is also called the segregated distribution model.
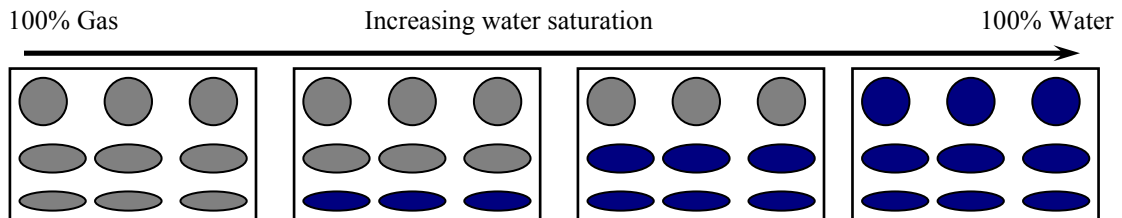
Figure (9): Segregated distribution or spheroid preference distribution model of three different aspect ratio pores. Gas = gray, Water = blue.

Measured velocities at high water saturation under the flow technique are higher than those computed by Biot-Geertsma equations. The X-ray measurements also showed nonuniformity of gas distribution at water saturation higher than 70%.

Domenico used the imbibition technique in order to improve the uniformity of gas fluid at high water saturation. The imbibition technique depends on injecting gas fluid first until gas fills the pores; then the rock sample is injected only with water. The fluid pressure was controlled in a way to let the gas turn to solution.

X-ray measurements showed the uniformity of water saturation as shown in Figure 10; gas bubbles are uniformly and homogeneously distributed in water.

31
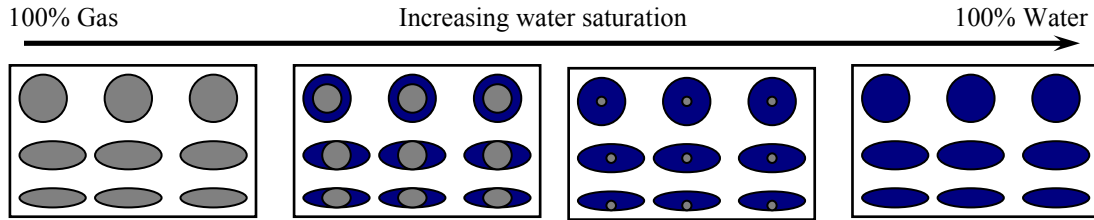
Figure (10): Uniform distribution model of three different aspect ratio pores. Gas = gray, Water = blue.

Domenico explained the difference in wave velocities between the measurements and the theoretical calculations by using the idea of microscopic distribution of the fluid phase inside the pores and the geometry of the fluid phase. He discovered that when the mixed fluids of gas and water in a pore space were uniformly distributed, there was an agreement between the measured and the calculated velocities. Domenico calculated the compressional and shear-wave velocities using the Biot-Gassmann equations modified by Geertsma (1961) (Equations 28 and 29). The calculated velocities were modeled for different values of the frame-fluid coupling factor (κ). Fluid compressibility (C_f), was calculated using the Wood-Ruess (Equations 13 and 30), which represent the weighted-by-volume average of gas compressibility plus water compressibility. The Wood-Ruess average assumes a uniform, homogeneous distribution. Domenico (1977) found that both measured P-wave and S-wave velocities are near the theoretical curve for a unity coupling factor (κ =1) at low and medium water saturation. However, at high water saturation, the measured velocities do not match the model of the Wood-Ruess average. Domenico assumed that at high water saturation the distribution of gas and water is not uniform anymore, and the fluid compressibility should be the inverse of the weighted-by-volume average; this was shown in Equations (15) and (16). Domenico concluded that effective fluid compressibility has values between the Reuss average, which is the lower

bound (gas and water have uniform distribution), and the Voigt average, which is the upper bound (gas and water have segregated distribution).

Murphy (1982) experimentally verified the uniform distribution model (lower bound) with the low frequency data on Massilon Sandstone. At high frequency the lower bound model cannot clarify the ultrasonic measurements, especially at high water saturation.

3.2.1.1 Physics and mathematics of uniform saturation

At low frequency and uniform distribution of a gas-water fluid, as a long wavelength passes through the saturated rock, it compresses the fluid phase, and an increase in pore pressure occurs in each pore. Because the wavelength is long, the pore pressure can equilibrate during the wave period. In the uniform distribution, the relaxation time (τ) is almost equal to the size of the fluid phase (L) over the diffusion constant (D), shown in Equation (32):

$$\tau \approx \frac{L^2}{D} \qquad , \qquad (32)$$

where τ = the relaxation time,

L = patch size or the spatial scale of fluid phase, and

D = diffusion constant.

The spatial scale (L) can be expressed in terms of the frequency (f) of the passing wave, and the diffusivity (D) seen in Equation (33):

$$L \approx \sqrt{D\tau} = \sqrt{\frac{D}{f}} \qquad . \qquad (33)$$

The diffusion constant is given by the next relation:

$$D = \frac{kK_{fl}}{\eta} \quad , \tag{34}$$

where k = permeability,

K_{fl} = fluid bulk modulus of the viscous fluid, and

η = dynamic viscosity of the liquid.

By substituting Equation 34 into Equation 33, the distance that pore pressure can equilibrate is given by Equation (35):

$$L \approx \sqrt{\frac{kK_{fl}}{f\eta}} \quad . \tag{35}$$

When the patches are small or the frequency is low, the pore pressure between the gas and water phases can be equilibrated. This is an isostress situation, because the pore fluid phase undergoes the same amount of pressure. The viscosity (η) and the permeability (k) of the fluid have an important impact on the value of (L). There are many relations similar to the previous equations reported in the geophysical literature such as White (1975); Akbar *et al*. (1994); Gist (1994); Mavko *et al*. (1997). At low frequency, the Biot and squirt flow mechanisms can be ignored (Mavko and Nur, 1975; O'Connell and Budiansky, 1977; Mavko and Jizba, 1991; Gist, 1994). At long wavelengths, there is time for the fluid pressure inside the pores of different aspect ratios to equilibrate. So at low frequencies, Biot's dispersion mechanism does not have that much effect on velocities compared to the effect at high frequencies. (The Biot and squirt mechanism are explained in Section 4.2.

Domenico (1976) indicated that the heterogeneous distribution of the fluid phase causes the difference in wave velocities between the measured and computed velocities at

high water saturation. The heterogeneity in saturation happens because the rock has variation in wettability, permeability, clay content, and pore shapes which affects the patch size or the fluid phase dimension.

The variation in saturation is called patchy saturation, and it has been considered theoretically by Endres and Knight (1991); Mavko and Nolen-Hoeksema (1994); Akbar *et al*. (1994); Knight *et al*. (1995); Packwood and Mavko (1995). The patchy saturation model was considered experimentally by Knight and Nolen-Hoeksema, (1990). In patchy saturation, the fluid is distributed in patches of fully gas-saturated and patches of fully water-saturated areas. Figure 11 shows how patchy saturation is distributed inside the pores of different aspect ratios.

100% Gas   Increasing water saturation   100% Water
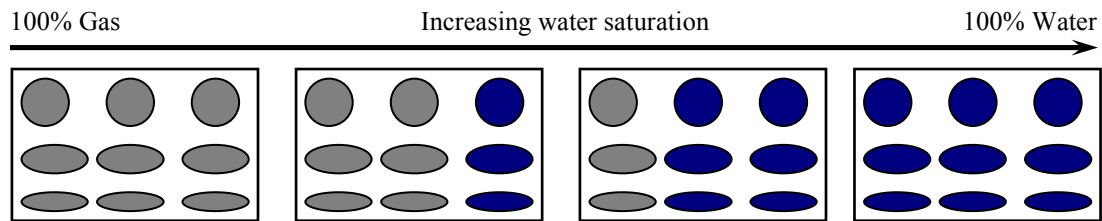
Figure (11): Patchy distribution model of three different aspect ratio pores. Gas = gray, Water = blue.

3.2.1.2 Physics and mathematics of patchy saturation

In patchy saturation, it is assumed that the porosity, the rock minerals, and the dry bulk modulus are homogenous. It is also assumed that the differences in velocities and moduli are caused by changes of pore fluid.

When the wavelength (λ) is long (low frequency) or when the patch size is not big, there is enough time for the produced pore pressure to equilibrate and diffuse through the wave period, seen in Equation (36):

$$L < \sqrt{\frac{k K_{fl}}{f \eta}} \qquad . \tag{36}$$

So the patches are relaxed, and this is the same as in the case of uniform saturation. However, when the wavelength (λ) is short (high frequency) or if the patch size is big, there is not enough time for the produced pore pressure to equilibrate and diffuse through the wave period, shown by Equation (37):

$$L > \sqrt{\frac{k\mathrm{K}_{fl}}{f\eta}} \qquad . \tag{37}$$

In this situation the patches are not relaxed, which means the effective bulk modulus is higher than the effective bulk modulus of the relaxed patches. So patchy saturation gives stiffer rock and higher velocities than uniform saturation. Also the Biot (1965) and squirt mechanisms (O'Connell and Budiansky, 1977) generate higher velocities at high water saturation.

Patchy saturation can be modeled under these three assumptions:
1) The shear modulus does not change with saturation; 2) The spatial scale size of the fluid is smaller than the wavelength; and 3) The patches should be of a size that cannot let the fluid pore pressure equilibrate through the wave period.

Under the previous assumptions, where the shear modulus is the same for all different patches, the effective bulk modulus of rock having patches of different shapes can be calculated by Equation (38) (Hill 1963):

$$K_{eff} = \left[\sum_{i=1}^{n} \frac{x_i}{K_i + \frac{4}{3}\mu} \right]^{-1} - \frac{4}{3}\mu \qquad , \tag{38}$$

where n = the number of patches with various fluid phase,

x_i = the volume portion of the ith patch,

K_i = the bulk modulus of the rock fully saturated with the ith fluid, and

μ = the shear modulus of the rock.

If the rock consists of two fluid phases like gas and water, Equation (38) can be expressed in terms of water and gas saturation by Equation (39):

$$K_{eff} = \left[\frac{S_{gas}}{K_{sat-gas} + \frac{4}{3}\mu} + \frac{S_w}{K_{sat-w} + \frac{4}{3}\mu} \right]^{-1} - \frac{4}{3}\mu \quad , \tag{39}$$

where S_{gas} = gas saturation,

$K_{sat-gas}$ = rock bulk modulus saturated with gas,

S_w = water saturation,

K_{sat-w} = rock bulk modulus saturated with water, and

μ = the shear modulus of the rock.

The saturated bulk moduli are calculated using Biot-Gassmann relations. The patchy saturation model ignores the effect of pore geometry. Pore geometry effects can exist and cause segregated saturation, which is not correctly modeled by using patchy saturation equations, especially at high water saturation and ultrasonic frequencies, for example (Endres and Knight, 1989; Castagna and Hooper, 2000).

Domenico (1977) found that the Voigt average fluid modulus is more applicable at high frequency and high water saturation. Experimentally, Endres and Knight (1989) verified the Domenico segregated distribution model by using the Kuster and Toksoz model for a variety of aspect ratio. The segregated model is more likely to happen at high frequency, and causes the shear modulus to vary with saturation. The effective fluid

bulk modulus of the segregated model is calculated using Equation (16) or (31). In any reservoir, the distribution of saturation is not known, and distribution varies from uniform (lower bound) to segregated distribution (upper bound) depending on many factors related to rock properties, such as permeability, fluid density and other factors like drilling, production, water injection rate, and gravity effects.

Mavko and Mukerji (1998) modeled low frequency data from Murphy (1982) on Massilon sandstone of porosity (ϕ=0.23). The results are in great agreement with the uniform effective fluid model (Reuss bound). However, the Mavko patchy model does not match Domenico's high frequency data on Ottawa unconsolidated sand. Also, the high velocity values at high water saturation are caused by the ultrasonic dispersion mechanism.

Chapter 4   ATTENUATION AND DISPERSION MECHANISMS IN FLUID-SATURATED ROCKS

In this chapter we will define attenuation and dispersion physically and mathematically; we also introduce macroscopic and microscopic dispersion mechanisms in partially saturated rocks.

4.1   Introduction and definitions

Attenuation is an important physical property that occurs in different materials like elastic solid and viscous materials. Visoelatic materials behave as elastic solids on short time range and as viscous fluids on long time range, thus exhibiting attenuation. Understanding how the attenuation mechanism is related to water saturation and pore shape can help in the interpretation of borehole sonic logs. Physically, attenuation is a dimensional measure of energy loss as a wave propagates through a scattering medium. The energy loss is caused by the motion between the pore fluid and the solid part of the rock, and also by the friction between the grain contacts, and both friction types cause the energy to convert to heat, which is physically called absorption.

Many studies have been done measuring attenuation in fluid-saturated rocks (Biot, 1956; White, 1965; Winkler, 1979; Murphy, 1982). Murphy (1982) proved that attenuation in very dry rocks is independent of frequency. However, attenuation is strongly dependent on frequency in fluid-saturated rocks. It is obvious that pore fluids dominate the energy loss in porous rocks. Mathematically, attenuation is expressed by the following relations, Equations (40) and (41) from (Sheriff 2002):

$$A = A_0 e^{-ax} \qquad , \qquad\qquad\qquad\qquad (40)$$

where A = wave amplitude,

A_0 = wave initial amplitude,

a = attenuation coefficient, and

x = traveling distance.

$$a = \frac{\pi f}{QV} \qquad , \qquad\qquad\qquad (41)$$

f = wave frequency,

Q = quality factor,

V = elastic wave velocity,

$\frac{1}{Q}$ = attenuation.

The quality factor over the seismic frequency range is assumed to be constant. While in the laboratory frequency range, the quality factor is frequency-dependent. Murphy (1982), proved the sensitivity of attenuation in partially gas- and water-saturated rocks. Pore fluid in laboratory measurements controls the attenuation mechanism. Frequencies are different at different scales; Figure 12 shows a frequency spectrum of different scales.

EARTHQUAKES   EXPLORTION   ECHO   BOREHOLE LAB

10^{-1} 10^{0} 10^{1} 10^{2} 10^{3} 10^{4} 10^{5} 10^{6}

SEISMIC   ACOUSTIC   ULTRASONIC
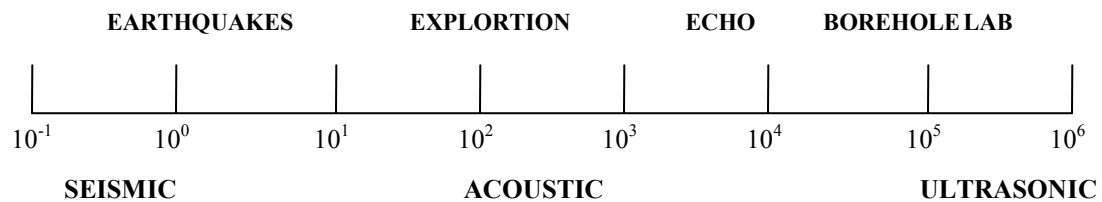
Figure (12): Frequency spectrum of geoacoustic interest in Hertz unit.

The energy loss in partially saturated rocks is explained by either the break of hydrogen bonds between the water molecules and the surface of the silicate gains or by viscous dissipation as the tiny water layer trapped in capillaries moves when the capillaries are compressed by a stress cycle. As water saturation increases, another dissipative mechanism controls the attenuation; this mechanism is the pore fluid flow, and it is frequency dependent. Murphy (1982) observed that the dependence of velocities and attenuation on the amount of water saturation changes as water saturation increases. The attenuation is higher at full-water saturation.

4.2   Biot's local flow mechanism

Biot (1956) was the first to consider the attenuation mechanism through the calculation of logarithmic decrements of compressional and shear-wave velocities. In high water-saturated porous media, he included the interaction between solids and fluids which is called local flow mechanism. Biot's local flow mechanism is a large-scale flow (macroscopic scale) between a pore fluid and a solid. Local flow mechanism is caused by a compressing wave which creates pore pressure that forces a fluid to flow related to solid motion. Biot's relations include the mass coupling factor that represents the effects of viscous friction and the inertial coupling forces between fluids and solids. Laboratory measurement observations (Murphy *et al*. 1982, 1986; Mavko and Jizba, 1991) predicted much larger velocities than those predicted by Biot, and the attenuation-dispersion magnitude was more likely to increase with increased frequency.

(Murphy *et al*. 1982, 1986; Mavko and Jizba, 1991; Akbar *et al*., 1993; and Dvorkin and Nur, 1993) involved another attenuation mechanism called squirt-flow; this is a small-scale flow at grain scale (microscopic scale), for example, a single pore.

41

When a rock frame is compressed by an acoustic wave, a high pore pressure is generated in the small aspect ratio microcrack. At high frequency (short wavelength) there is not enough time for pore pressure to equilibrate during the wave period, and thus the rock bulk and shear moduli are stiffer. At partial saturation, the low bulk modulus of the fluid gas and water mixture generates different pore pressure gradients at different pore shapes. Higher velocities will be produced from the non-uniformity of the stress cycle in different pores.

Chapter 5   METHODS

In this chapter we will introduce a simple method in order to ignore the effect of the squirt-flow dispersion mechanism at full-water saturation, and a new distribution model called patchy segregation. Many mathematical calculations will be described in detail for each step.

5.1   Introduction

Compressional and shear-wave velocities versus gas-water saturation curves have been modeled in different approaches using different fluid distribution models. Models fitting saturation curves with elastic wave velocities reported in the literature are incomplete and have some discrepancies between each other, for example, with Ottawa sand (Domenico, 1977; Mavko and Mukerji, 1998). Also in the literature correction for the dispersion and attenuation mechanisms is not complete and is applied to all types of porous rocks (Domenico, 1977; and Gregory, 1977). So the measured velocities are not in agreement with the theoretical models.

The methods fitting ultrasonic velocities versus saturation curves we present in this thesis compensate for the experimental and theoretical errors and discrepancies found in published data in the geophysical literature.

5.2   Curve fitting steps

5.2.1   Using Biot-Geertsma equations

The curve fitting begins by using Biot's theory (1956) to calculate wave velocities in rocks which contain mixed partial fluid saturation. Geertsma (1961) extended another expression for compressional-wave velocity as a function of frequency. The Biot-Geertsma relation is considered a reasonable starting point since Biot relations give a

good estimation of wave velocity in porous rocks containing more than one fluid. A mixed fluid can be considered as a single fluid phase with an effective fluid bulk modulus. The Biot-Geertsma equations given in Equations (42) and (43) are the same as Equations (28) and (29):

$$V_P = \left\{ \left[\left(\frac{1}{C_b} + \frac{4}{3}\mu \right) + \frac{\frac{\phi\rho_b}{\kappa\rho_f} + (1-\beta)(1-\beta-2\phi/\kappa)}{(1-\phi-\beta)C_s + \phi C_f} \right] \cdot \frac{1}{\rho_b\left(1 - \frac{\rho_f\phi}{\rho_b\kappa}\right)} \right\}^{\frac{1}{2}} \quad ; \qquad (42)$$

$$V_s = \left(\frac{\mu}{\rho_b(1 - \frac{\rho_f\phi}{\rho_b\kappa})} \right)^{\frac{1}{2}} . \qquad (43)$$

5.2.2   Using porosity separation

The fitting method starts from matching the ending point of the curves (at full-water saturation), because there is high velocity dispersion at full water saturation. When the ending points of both models are matched, the data between the starting and the ending points can be fit correctly using fluid distribution models. The fitting methods begin with the measured compressional and shear wave velocities at full-gas saturation, and thus the starting point of the models is the same (with careful consideration of gas compressibility under pressure).

Matching the end point of the theoretical model with the measured model can be done by applying the porosity separation method, which includes the separation of the total porosity into acoustically connected and disconnected parts.

It is known that total porosity (ϕ_T) consists of connected pores (ϕ_c) and disconnected pores (ϕ_D), shown by Equation (44):

$$\phi_{Total} = \phi_{Connected} + \phi_{Disconnected} \qquad . \qquad (44)$$

The connected porosity represents the permeable pores that are connected with each other, while the disconnected porosity represents impermeable pores that are isolated and not connected with each other; this is shown in Figure 13.

Permeability is a very important parameter because it controls the motion of fluid between pores. So by separating the total porosity of connected and disconnected pores, the effect of fluid motion can theoretically be controlled and give the freedom to control the theoretical model at full water saturation. Also the effect of Biot's local flow can be ignored, and no correction is required for the dispersion effects, since the permeability is controlled by the separation of the total porosity.

Permeable pore

(Connected porosity)

Impermeable pore throats
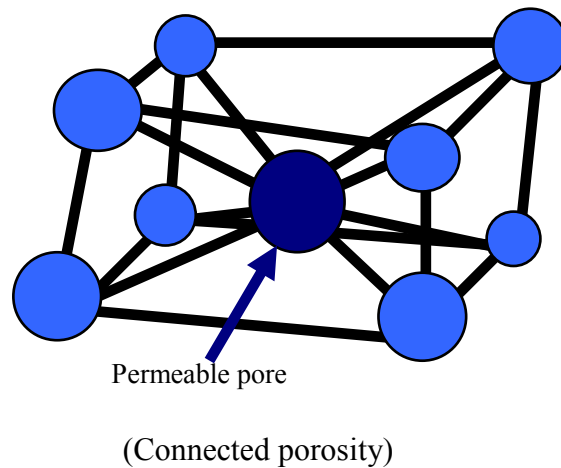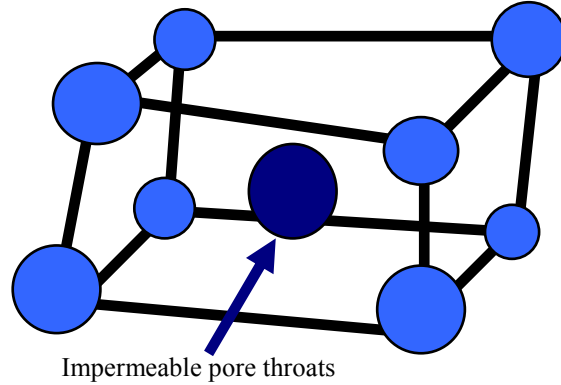
(Disconnected porosity)

Figure (13): Sketch of connected and disconnected porosity.

5.2.2.1 Mathematics of porosity separation

Porosity separation begins by using velocity-porosity empirical relations. Raymer-Hunt-Gardner relations (Mavko, 1998) will be used in order to estimate the velocities of rocks with given minerals and pore fluid. The Raymer *et al*. relations assume that the rock is isotropic, fluid-saturated, has uniform minerals, and is under high effective pressure. These relations work well for low- and medium-porosity rocks:

$$V_{Psolid} = (1 - \phi_d)^2 V_{Pmatrix} + \phi_d V_{Pfluid} \qquad , \qquad (45)$$

where V_{Psolid} = compressional wave velocity of the solid rock,

$V_{Pmatrix}$ = compressional wave velocity of the matrix,

V_{Pfluid} = compressional wave velocity of the fluid, and

ϕ_d = disconnected porosity which is given by the difference between the total and connected porosity, Equation (46).

$$\phi_d = \phi_T - \phi_C \qquad . \qquad (46)$$

The disconnected pores can be considered as part of the solid minerals of the rock, and a new compressibility value of the solid grains should be used in the calculation of the effective bulk modulus.

The calculated (V_{Psolid}) from Equation (45) is used to compute the effective compressibility of the solid minerals (C_s^*), which is a major parameter in Biot's equation. The effective compressibility of the solid minerals is given in Equation (47):

$$C_s^* = \frac{1}{\rho_{matrix}(V^2_{Psolid} - \frac{4}{3}\mu_{matrix})}$$

(47)

where ρ_{matrix} = density of the matrix (solid grains),

V_{Psolid} = compressional wave velocity of the solid rock, and

μ_{matrix} = shear modulus of the matrix (solid grains).

Using the effective compressibility of the solid minerals in Biot's high frequency compressional wave velocity equation, we can control the ratio of connected to total porosity, which is a variable number that can be changed until the best fit of the ending point can be achieved.

5.2.2.2. Mathematics of bulk and shear modulus

The effective bulk modulus (K_{sat}) in the Biot-Geertsma equation has many parameters, as given in Equation (48):

$$K_{sat} = \frac{1}{C_b} + \frac{\frac{\phi_c\rho_b}{\kappa\rho_f} + (1-\beta)(1-\beta-2\phi_c/\kappa)}{(1-\phi_c-\beta)C_s^* + \phi_c C_f} .$$

(48)

From Equation (48), (ϕ_c) is the connected porosity, which is equal to the total

porosity if there is no separation. When the total porosity (ϕ_T) is separated, the ratio of

connected to total will be different and the disconnected porosity will be part of the solid.

By using the effective compressibility of matrix solid, the disconnected porosity (ϕ_d) can

be isolated from the action of fluids in permeable pores. (C_s) is the compressibility of the

solid material. In quartz sand, the solid compressibility is equal to 0.027Gpa, (C_s^*) is the

effective compressibility of the solid material, (β) is the ratio of the effective grain

compressibility to the dynamic frame compressibility, (C_s^*/C_b), (ρ_b) is the rock total

bulk density which is given by Equation (8), (ρ_f) is the density of the pore fluid which

can be computed from Equation (9), and (C_f) is the compressibility of the pore fluid

which will be calculated differently according to the type of saturation distribution.

A (C_f) of uniform distribution can be calculated by the Reuss average from Equation

(30), while a (C_f) of segregated distribution can be computed by the Voigt average from

Equation (31). So the saturated bulk modulus will have two different values, one for

uniform distribution, and the other for segregate distribution. The saturated bulk modulus

of the simple patchy and patchy segregation is computed separately by Equation (39). (κ)

is the mass coupling factor between the fluid and solid, it is a free parameter of the curve

matching and has a value of one or more at ultrasonic frequencies. Different values of the

mass coupling factor will be used in Biot's equations in order to fit ultrasonic velocities

versus water-gas saturation, to understand the effect of mass coupling on the shape of the

curves and to compensate for the error in the assumed coupling factor value at ultrasonic

measurements. The effective bulk modulus calculation begins with the frame bulk modulus or the frame compressibility (C_b). This is called the dynamic frame compressibility because it is computed from the dynamic measured compressional and shear-wave velocities by:

$$C_b = \frac{1}{\rho_b(V_p^{\,2} - \frac{4}{3}V_s^{\,2})} \quad ,$$ (49)

where ρ_b = rock total bulk density,

V_p = dynamic measured compressional velocity at full-gas saturation, and

V_s = dynamic measured shear velocity at full-gas saturation.

Before applying the velocity equations, we should identify the effective shear modulus. We assume that the dry and saturated shear moduli are equal, and the shear modulus is independent of saturation. Because the dynamic measured shear velocity is known, the shear modulus can be calculated from Biot shear-wave velocity at infinite frequency, with Equations (29) or (50), since Geertsma did not develop relations for shear-wave velocity:

$$\mu_{eff} = V_S^{\,2}\rho_b\left(1 - \frac{\rho_f\phi_c}{\rho_b\kappa}\right) \quad ,$$ (50)

where V_S = measured shear velocity at full-gas saturation,

ϕ_c = connected porosity,

ρ_f = density of pore fluid, and

ρ_b = rock total bulk density.

After the calculation of saturated bulk and shear moduli, the compressional and shear-wave velocities are computed from the following equations:

$$V_P = \left[\frac{K_{sat}}{\rho_b \left(1 - \frac{\rho_f \phi}{\rho_b \kappa} \right)} + \frac{4}{3} \mu_{eff} \right]^{\frac{1}{2}} \quad \text{and} \tag{51}$$

$$V_s = \left(\frac{\mu_{eff}}{\rho_b \left(1 - \frac{\rho_f \phi}{\rho_b \kappa} \right)} \right)^{\frac{1}{2}} . \tag{52}$$

The uniform and fully segregated models are computed separately using different effective fluid compressibilities. The patchy model represents partially segregated model.

5.2.3 Using the patchy segregation model

The fitting methods include the three theoretical models of fluid-phase distribution: the uniform, the segregated, and the simple patchy. The mathematical calculations of the three models were explained in Chapter 3. The new model in the fitting method is the patchy segregation model. The patchy segregation model represents the intermediate fluid distribution between the uniform and the fully segregated distribution. Mathematically, patchy segregation can be modeled by applying the same calculation as for the simple patchy, but the starting and ending points of the effective bulk moduli are different. The effective bulk modulus is given by the reciprocal average of moduli of shared regions of uniform and fully segregated distribution, as in Equation (53).

$$K_{eff} = \left[\frac{S_{gas}}{K_{sat-uniform} + \frac{4}{3}\mu} + \frac{S_w}{K_{sat-segregated} + \frac{4}{3}\mu} \right]^{-1} - \frac{4}{3}\mu_{eff} \quad , \tag{53}$$

where S_{gas} = gas saturation,

$K_{sat-uniform}$ = saturated bulk modulus of the uniform region,

S_w = water saturation,

$K_{sat-segregated}$ = saturated bulk modulus of the segregated region, and

μ_{eff} = effective shear modulus of the rock.

Equation (51) is the same equation as that of the simple patchy (Equation 38) except that the starting and ending points are different; also the values of saturation at the starting and ending point are different. Physically, the patchy segregation distribution appears as patches of uniform distribution and patches of segregated distribution, as shown in Figure 14.

100% Gas   Increasing water saturation   100% Water
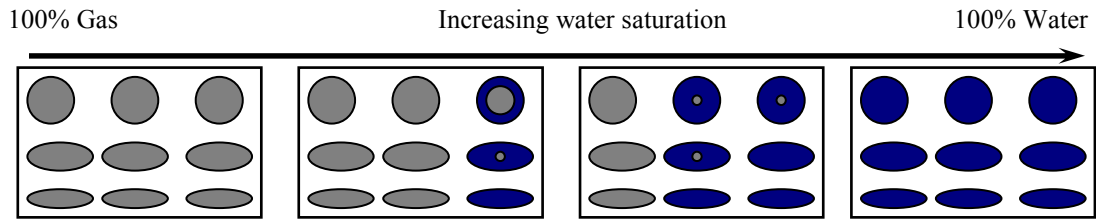
Figure (14): Patchy segregation model of three different aspect ratio pores.

The patchy segregation model can explain the transitional zones of measured data that do not fit in the three theoretical models of uniform, segregated, and simple patchy distribution. Applying the step just described, measured ultrasonic velocities versus saturation can be matched exactly with the theoretical models of Biot. The methods can be applied on different type of sedimentary rocks.

Chapter 6   MODELING AND INTERPRETING MEASURED AND COMPUTED ULTRSONIC VELOCITIES

We have modeled six types of rocks at different porosity values from high, medium, and small. All the data are taken from published literature.   The interpretation of each velocity model will be described after modeling each rock separately.

6.1   Introduction

This chapter analyzes published geophysical laboratory data on different partially saturated rocks, as presented in Table (1). The published laboratory velocity data are compared, modeled and interpreted with our method.

Samples (*Reference*)	f (kHz)	ϕ	k (mD)	ρ_s (g/cm^3)	K_s (GPa)	ρ_w (g/cm^3)	K_w (GPa)	ρ_g (g/cm^3)	K_g (GPa)
Ottawa Sands *Domenico (1977)*	500	0.383	2400	2.65	37	1.13	2.49	0.00129	0.00014
Glass Beads *Domenico (1977)*	500	0.383	1900	2.42	37	1.13	2.49	0.00129	0.00014
Boise Sandstone *Gregory (1976)*	1000	0.268	1000	2.65	37	1.00	2.23	0.00129	0.00014
Spirit River TGS *Knight and Nolen-Hoeksema (1990)*	1000	0.052	0.001	2.65	37	1.00	2.23	0.00129	0.00014
Sierra White Granite *Murphy (1985)*	200	0.008	0.001	2.65	56	1.00	2.23	0.00129	0.00014

Table 1. Sample properties used in the calculation of the modeled velocities versus saturation curves.

In Table 1, (f) is the frequency of the acoustic measurements in kHz unit, (ϕ) is the total porosity, (k) the permeability in milidarcy unit, (ρ_s) is the grain density in gram/cm^3 unit, (K_s) is the grain bulk modulus in Giga-Pascal unit, (ρ_w) is the water density in gram/cm^3 unit, (K_w) is the water bulk modulus Giga-Pascal unit, (ρ_g) is the gas density gram/cm^3, and (K_g) is the gas bulk modulus Giga-Pascal unit. All the values of fluid density and fluid bulk moduli are under standard conditions of temperature and pressure (20° C, 1 atmospheric pressure). The pore fluid is (150,000) ppm NaI brine for glass beads and Ottawa sand, and distilled water for consolidated and low-porosity rocks.

6.2 High porosity rocks, unconsolidated sand (Ottawa sand, and glass beads)

Two samples of unconsolidated rock (Ottawa sand and glass beads) were used by Domenico (1977) to measure ultrasonic velocities at a frequency of 500 kHz. The imbibition and flow techniques were applied in injecting the fluid in order to create partial saturation. In the imbibition technique, the fluid has more uniform distribution than the flow technique, which exhibited heterogeneous distribution. The flow technique depends on mixing the water and gas before injection. The saturation in the Ottawa sand sample was created using the flow technique, while the saturation in the glass beads was created using both flow and imbibition techniques. The measured velocity data were taken from Domenico (1977).

6.2.1 Ottawa sand

Domenico (1977) measured ultrasonic velocities in Ottawa sand, as shown in Figure 15, using the flow technique. Ottawa sand consists of very fine, angular, pure quartz grain with high porosity and permeability.

53

Taken from Domenico 1977
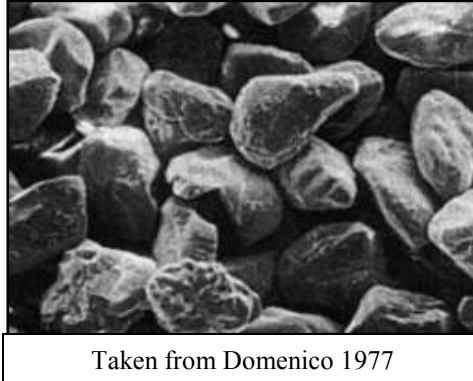
Figure (15): Scanning-electron-microscope photograph of Ottawa sand.

The velocities were measured at different differential pressures (1500 and 4500 psi). The measured velocity data under a differential pressure of 1500 psi is listed in Table 2, after it was converted from ft/sec to Km/sec.

Average water saturation (S_w)	Compressional wave velocity V_P (Km/s)	Shear wave velocity V_S (Km/s)
0	1.255	0.836
0.504	1.255	0.829
0.556	1.266	0.829
0.667	1.260	0.827
0.865	1.294	0.813
0.939	2.030	0.783
0.974	2.060	0.802
1	2.072	0.801

Table 2. Ottawa-sand specimen measured velocities versus average water saturation under differential pressure (P_d=1500psi) from Domenico (1977).

6.2.1.1 Modeling and interpreting measured and computed ultrasonic velocity models

6.2.1.1.1 Modeling the compressional wave velocities (P-wave)

All calculations for compressional and shear-wave velocities were coded using Microsoft Excel software. The beginning of the velocity calculations starts from the measured data. First, we calculated the dynamic shear modulus (μ) from the measured

shear velocity at full-gas saturation by Equation (50). The shear modulus was assumed to be independent of saturation. The dry and the wetted shear moduli are equal: ($\mu_{Dry} = \mu_{wet}$). The shear modulus varies with the mass coupling factor (κ). The input and output parameters in calculating the effective shear modulus are listed in Table 3. The value of gas density is different at pressure (1500 psi). The fluid density (ρ_f) was computed from Equation (9), and the bulk density (ρ_b) was computed from Equation (8).

Input at $S_w = 0$					Output
ρ_f (g/cm³)	ρ_b (g/cm³)	V_S^2 (km/s)	$\emptyset$	κ	μ (Gpa)
0.132	1.66	0.699	0.383	1	1.143
0.132	1.66	0.699	0.383	1.5	1.149
0.132	1.66	0.699	0.383	2	1.152
0.132	1.66	0.699	0.383	2.5	1.154
0.132	1.66	0.699	0.383	3	1.166
0.132	1.66	0.699	0.383	11	1.175
0.132	1.66	0.699	0.383	∞	1.177

Table 3. Calculations of the dynamic shear modulus at different values of mass coupling factor in Ottawa sand at full gas saturation.

The shear modulus increased as the mass coupling facto increased. After the shear modulus was determined, the calculation of the effective bulk modulus (K_{sat}) began. From Equation (48), the input parameters were calculated starting with the frame compressibility. (C_b) was computed from the measured compressional and shear velocities by Equation (49). The rock bulk density increased with water saturation since the density of water is higher than gas. Some input parameters are listed in Table 4.

ρ_w (g/cm^3)	ρ_g (g/cm^3)	$\varnothing$	C_b (Gpa^{-1})	C_s (Gpa^{-1})	$\beta = C_s/C_b$	(1-β)
1.13	0.132	0.383	0.9	0.027	0.03	0.97

Table 4.Ottawa sand parameters used to calculate the effective bulk modulus.

The effective fluid compressibility (C_f) was calculated separately by Equations (30) and (31), and represents the Reuss and Voigt averages. The fluid compressibilities were computed separately using the values in Table (1) while considering the changing in pressure and temperature.

S_w	Reuss K_{sat} (Gpa)	Voigt K_{sat} (Gpa)	Simple Patchy K_{sat} (Gpa)
0	1.119	1.119	1.119
0.05	1.115	2.344	1.210
0.1	1.113	3.079	1.308
0.2	1.110	3.964	1.526
0.4	1.109	4.926	2.082
0.6	1.111	5.536	2.884
0.65	1.112	5.664	3.144
0.7	1.114	5.786	3.437
0.73	1.115	5.856	3.630
0.76	1.116	5.925	3.840
0.8	1.119	6.014	4.147
0.82	1.121	6.057	4.314
0.84	1.123	6.100	4.491
0.86	1.126	6.142	4.680
0.88	1.130	6.183	4.881
0.9	1.135	6.225	5.095
0.92	1.143	6.265	5.324
0.94	1.157	6.305	5.569
0.96	1.184	6.345	5.832
0.98	1.264	6.384	6.116
0.99	1.416	6.403	6.267
0.992	1.489	6.407	6.297
0.994	1.606	6.411	6.328
0.996	1.823	6.415	6.360
0.998	2.372	6.419	6.391
0.999	3.153	6.421	6.407
1	6.423	6.423	6.423

Table 5. Results of calculated effective bulk moduli of uniform, segregated, and patchy saturation distribution in Ottawa Sand.

When all the input parameters were computed, the output is effective bulk moduli of Reuss (uniform distribution), Voigt (fully segregated distribution), and patchy (simple segregation distribution.) The saturated bulk modulus of the simple patchy was computed separately from Equation (38), (Hill 1963). The three different effective bulk moduli versus saturation results are listed in Table 5.

S_w	ρ_f (g/cm^3)	ρ_b (g/cm^3)	Reuss V_P (km/s)	Voigt V_P (km/s)	Simple Patchy V_P (km/s)
			μ = 1.143 (Gpa)		
0	0.132	1.686	1.271	1.271	1.271
0.05	0.182	1.705	1.270	1.538	1.293
0.1	0.232	1.724	1.270	1.678	1.316
0.2	0.332	1.762	1.269	1.832	1.366
0.4	0.531	1.838	1.269	1.986	1.485
0.6	0.731	1.915	1.270	2.078	1.642
0.65	0.781	1.934	1.270	2.097	1.690
0.7	0.831	1.953	1.270	2.114	1.742
0.73	0.861	1.965	1.270	2.125	1.775
0.76	0.890	1.976	1.271	2.134	1.811
0.8	0.930	1.991	1.271	2.147	1.862
0.82	0.950	1.999	1.272	2.153	1.890
0.84	0.970	2.007	1.272	2.159	1.918
0.86	0.990	2.014	1.273	2.165	1.948
0.88	1.010	2.022	1.274	2.171	1.979
0.9	1.030	2.030	1.275	2.177	2.012
0.92	1.050	2.037	1.277	2.183	2.046
0.94	1.070	2.045	1.281	2.188	2.083
0.96	1.090	2.053	1.287	2.194	2.121
0.98	1.110	2.060	1.306	2.199	2.162
0.99	1.120	2.064	1.341	2.202	2.183
0.992	1.122	2.065	1.357	2.202	2.187
0.994	1.124	2.066	1.383	2.203	2.191
0.996	1.126	2.066	1.431	2.204	2.196
0.998	1.128	2.067	1.544	2.204	2.200
0.999	1.129	2.067	1.691	2.204	2.202
1	1.130	2.068	2.205	2.205	2.205

Table 6. Results of computed P-wave velocities versus saturation of the uniform, segregated, and simple patchy in Ottawa sand.

The compressional wave velocities are calculated from Biot's high frequency Equations (51). The computed bulk moduli were calculated at a mass coupling factor equal to one ($\kappa=1$), and at a connected-to-total porosity ratio equal to one ($\phi_c=\phi_T$). The computed compressional wave velocity results of the three different distribution models are listed in Table 6.

The computed and measured compressional wave velocities as a function of water saturation were modeled using Microsoft Excel software. Figure 16 shows the Ottawa sand velocity curves versus water saturation of both measured and computed compressional wave velocities.

Figure (16): Results of P-wave velocity models in Ottawa sand as a function of water saturation from Domenico (1977) at coupling factor of one ($\kappa=1$), porosity ratio of one ($\phi_c/\phi_T=1$), and deferential pressure of 1500 psi.

The ending point of the theoretical computed models at full water saturation (S_w = 1) did not match the measured velocity. Measured velocities were in good agreement with the uniform model on saturation range from full gas saturation (S_w = 0) to high water saturation (S_w = 0.85). The ratio of connected to total porosity of 1 did not match the ending point of the models. If the ratio of connected to total porosity takes a different value, then the ending point can be matched. Also changing the value of the mass coupling factor can add more accuracy in fitting the models, since the assumed value of coupling could be inaccurate. However, when the mass coupling factor increases to a value of 2.5 (κ = 2.5), the ending point matched with the measured velocities at high water saturation, but there was a violation with the uniform model for the rest of the measured values from S_w =20% to S_w = 80%.

6.2.1.1.2 Correcting compressional wave velocity models

As the ratio of connected-to-total porosity was changing, there was a potential to fit the ending point. Different ratios were used until the best fit was achieved. The best fit was achieved at ratio of connected-to-total porosity of 0.75 (ϕ_c / ϕ_T =0.75), which means that 25% of the total porosity was disconnected and considered as part of the solid grain compressibility (C_s). Table 7 has the new parameters separating the total porosity.

ρ_w (g/cm^3)	ρ_g (g/cm^3)	$\varnothing_c$	C_b (Gpa^{-1})	C^*_S (Gpa^{-1})	$B=C_s/C_b$	$(1-\beta)$
1.13	0.132	0.28725	0.9	0.102	0.11	0.89

Table 7. Ottawa sand new parameters used to calculate the effective bulk moduli.

After repeating the same steps from the previous calculations, the velocities were computed and then modeled. Figure 17 show the velocity curves of the P-wave velocities according to the porosity separation method.

Figure (17): Curve fit of P-wave velocity models in Ottawa Sands as a function of water saturation from Domenico (1977) at a differential pressure of 1500 psi. Curve fit parameters include a coupling factor of one, connected-to-total porosity ratio of 0.7. Solid circles are saturations established using the flow technique.

6.2.1.1.3 Interpreting compressional wave velocity models

The measured data fit the uniform model at high saturation range, starting from full-gas saturation ($S_w = 0\%$) to high water saturation ($S_w = 85\%$). The measured data fit the uniform model because Ottawa sand has high permeability and porosity. So the pore pressure has time to equilibrate, and also the fluid can move freely between the pores of different shapes. At ($S_w = 0.9$) the measured P-wave velocity suddenly jumped to violate

the patchy model and match the fully segregated model. There is no transitional zone for the measured data from the uniform model to the fully segregated model.

The rapid change in velocity at high-water saturation can be fit using the patchy segregation model which represents the intermediate zone between uniform and segregated distribution. The patchy segregation was modeled using Equation (53). The effective bulk modulus and the compressional wave velocity of the patchy segregation are listed in Table 8.

S_w	$K_{Uniform}$	$K_{Segregated}$	$K_{uni}+4/3\mu$	$K_{seg}+4/3\mu$	ρ_b	$4/3\,\mu$	K_{eff}	V_P
0.86	1.14	5.843	2.676	7.379	1.73	1.536	1.4	1.285
0.93	1.177	5.933	2.713	7.469	1.77	1.536	5.915	2.037

Table 8. Calculations of the patchy segregation model in Ottawa sand.

The transitional zone starts at $S_w = 0.85$ and ends at $S_w = 0.94$, so the value of saturation is 0 at $S_{uniform}$ and 1 at $S_{segregated}$, and the value of saturation between the starting and ending point, will be interpolated as a percentage value on the saturation range between 0.85 and 0.94; for example, at $S_w = 0.86$, the value should be in the equation equal to 0.1, while at the $S_w = 0.93$ it should be equal to 0.98. The measured velocity at full-water saturation in Ottawa sand jumped from the starting point to the ending point of the patchy segregation model. Because Ottawa sand has a high permeability and porosity there is no major transitional zone. Figure (18) shows the last results of fitting the measured compressional wave velocity data with the theoretical models in Ottawa sand.
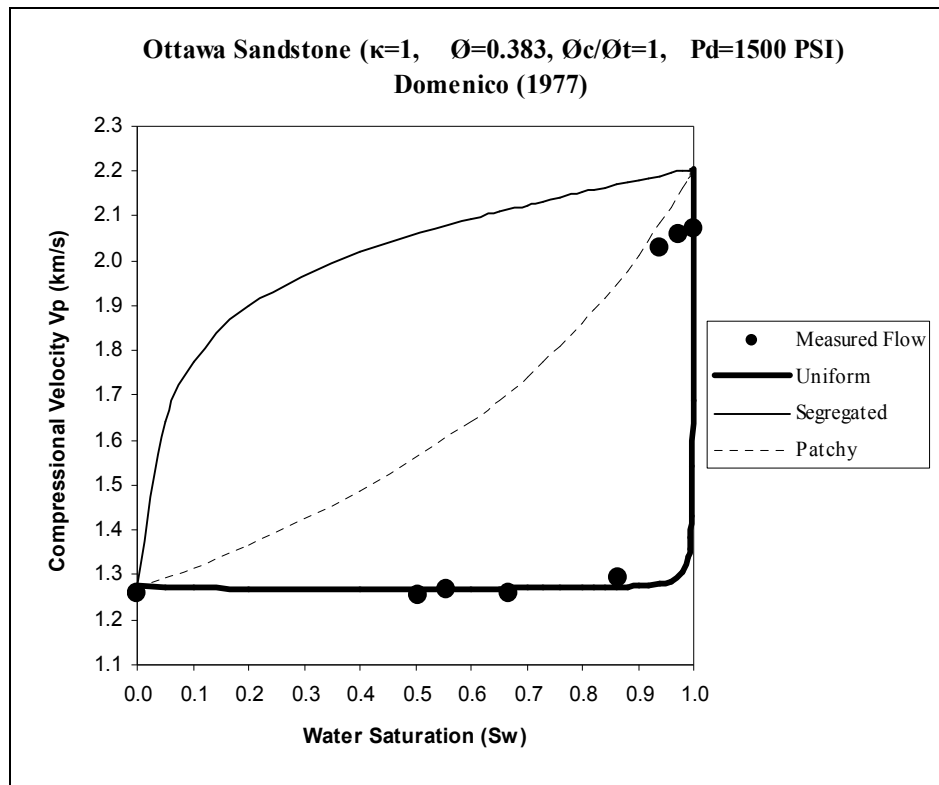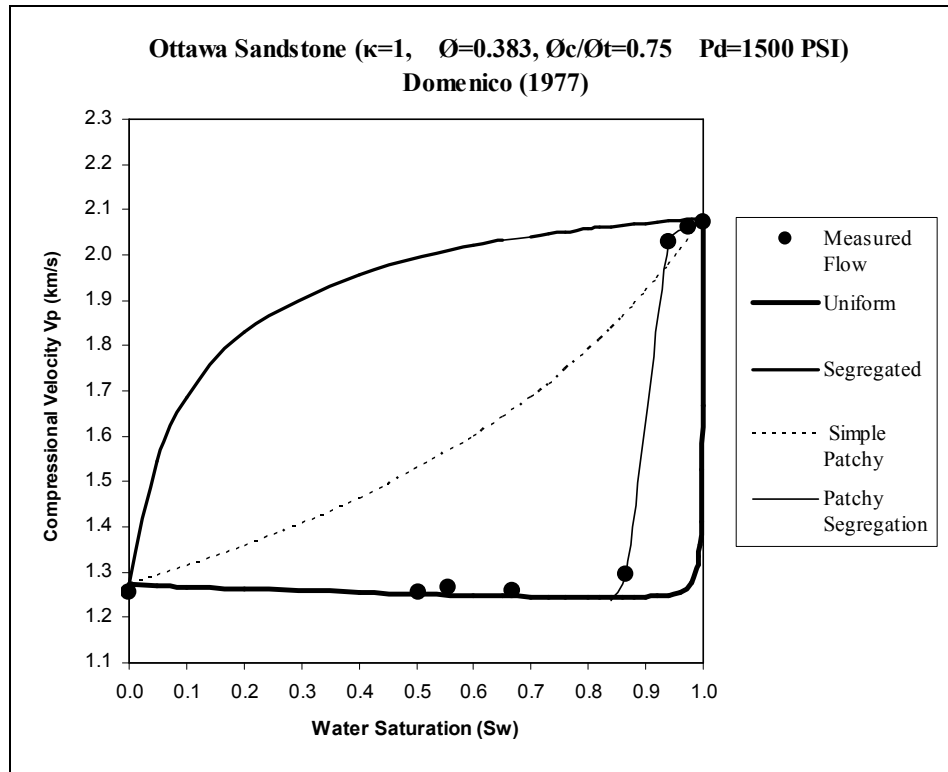
Figure (18): Curve fit of P-wave velocity models in Ottawa sands as a function of water saturation from Domenico (1977) at a differential pressure of 1500 psi. Curve fit parameters include coupling factor of one, connected-to-total porosity ratio of 0.75, and patchy segregation model in the transitional zone from $S_w = 85\%$ to 94%. Solid circles are saturations established using the flow technique.

6.2.1.1.4 Modeling the shear-wave velocities (S-wave)

The shear-wave velocities are computed from the Biot high-frequency equation (52), since Geertsma did not develop equations for shear-wave velocity. The computed shear velocities versus saturation are computed for different values of mass coupling factor from one to infinite. Results are listed in Table (9).

6.2.1.1.5 Interpreting shear-wave velocity models

From Figure (19), shear-wave velocities were modeled versus water saturation at four values of mass coupling factor. The measured values were in good agreement with the theoretical models at mass coupling factor of ($\kappa =1$, $\kappa=2$). The shear velocity decreased linearly with increasing saturation, because fluid density increased. Shear-

wave velocity was very sensitive to fluid distribution. The flow technique caused non-uniformity in the shear-wave velocity behavior.

S_w	ρ_f (g/cm^3)	ρ_b (g/cm^3)	$\kappa = 1$ $\mu=1.143$ (Gpa)	$\kappa = 1.5$ $\mu=1.155$ (Gpa)	$\kappa = 3$ $\mu= 1.66$ (Gpa)	$\kappa = \infty$ $\mu= 1.77$ (Gpa)
			V_S (km/s)	V_S (km/s)	V_S (km/s)	V_S (km/s)
0	0.132	1.662	0.836	0.836	0.836	0.836
0.05	0.182	1.682	0.836	0.835	0.833	0.831
0.1	0.232	1.702	0.836	0.833	0.830	0.827
0.2	0.332	1.743	0.836	0.830	0.823	0.818
0.4	0.531	1.824	0.836	0.824	0.811	0.801
0.6	0.731	1.905	0.836	0.817	0.800	0.785
0.65	0.781	1.926	0.836	0.816	0.797	0.781
0.7	0.831	1.946	0.836	0.814	0.795	0.778
0.73	0.861	1.958	0.836	0.814	0.793	0.775
0.76	0.890	1.970	0.836	0.813	0.791	0.773
0.8	0.930	1.987	0.836	0.812	0.789	0.770
0.82	0.950	1.995	0.836	0.811	0.788	0.769
0.84	0.970	2.003	0.836	0.810	0.787	0.767
0.86	0.990	2.011	0.836	0.810	0.786	0.766
0.88	1.010	2.019	0.836	0.809	0.785	0.764
0.9	1.030	2.027	0.836	0.809	0.784	0.763
0.92	1.050	2.035	0.836	0.808	0.783	0.762
0.94	1.070	2.043	0.836	0.807	0.782	0.760
0.96	1.090	2.052	0.836	0.807	0.781	0.759
0.98	1.110	2.060	0.836	0.806	0.780	0.757
0.99	1.120	2.064	0.836	0.806	0.779	0.757
0.992	1.122	2.065	0.836	0.806	0.779	0.757
0.994	1.124	2.065	0.836	0.806	0.779	0.756
0.996	1.126	2.066	0.836	0.806	0.779	0.756
0.998	1.128	2.067	0.836	0.806	0.779	0.756
0.999	1.129	2.067	0.836	0.806	0.779	0.756
1	1.130	2.068	0.836	0.806	0.779	0.756

Table 9. Results of computed S-wave velocities versus saturation in Ottawa sand at different coupling factor values.

Ottawa Sandstone (Ø=0.383, Øc/Øt=1, Pd=1500 PSI)
Domenico (1977)

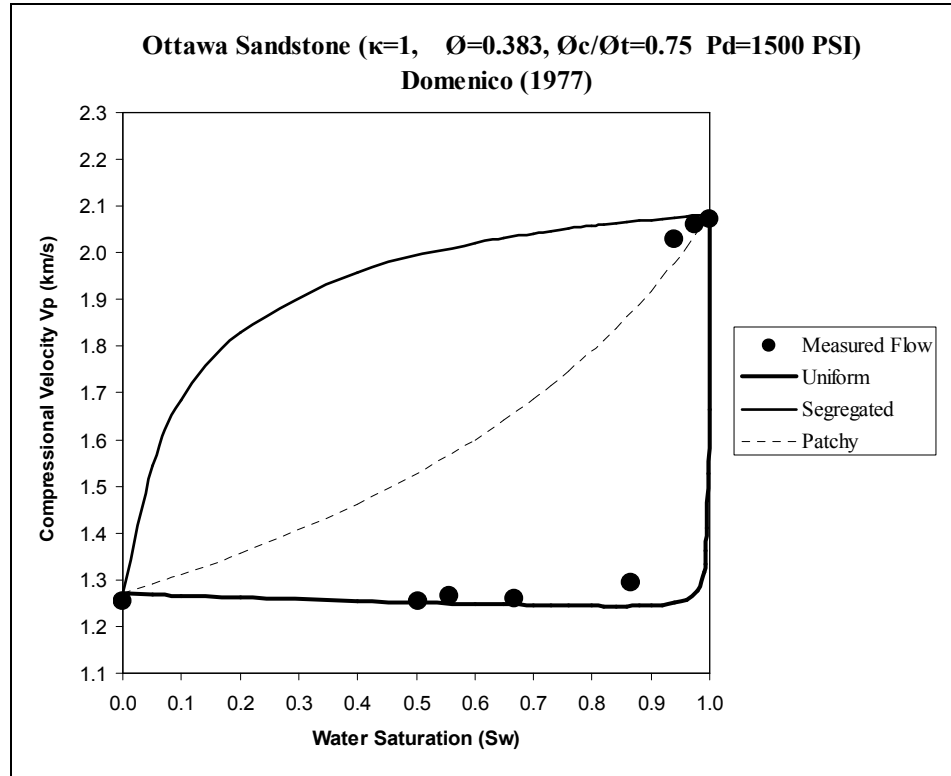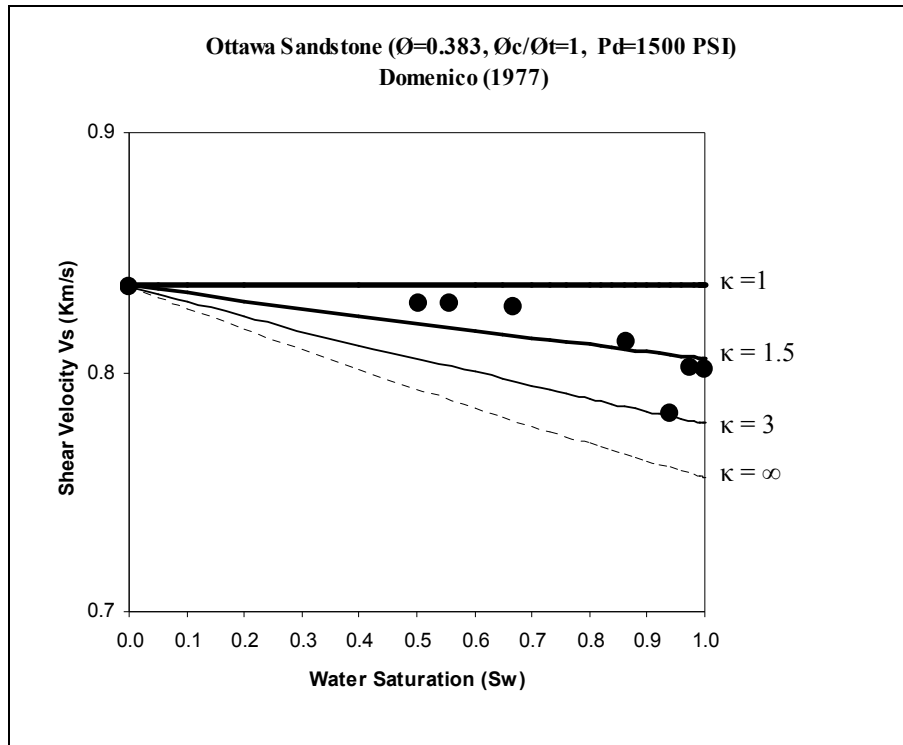Figure (19): Curve fit of S-wave velocity in Ottawa sand as a function of water saturation from Domenico (1977) at coupling factor of (κ =1, 1.5, 3, ∞) and pressure of 1500 psi. Solid circles are saturations established using a flow technique.

6.2.2 Glass Beads

Domenico (1977) also measured ultrasonic velocities in another unconsolidated sample, spherical glass beads, which have almost the same porosity and compressibility of Ottawa sands. The only difference is the grain density, grain shape, and pore size; the glass beads are shown in Figure 20.
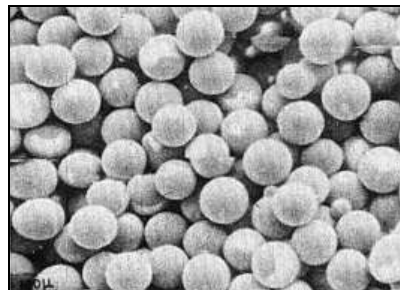
Taken from Domenico 1977

Figure (20): Scanning-electron-microscope photograph of glass beads

64

Average water saturation (S_w)	Compressional wave velocity V_p (Km/s)	Shear wave velocity V_s (Km/s)
0.887	1.1064	0.673
0.947	1.143	0.635
0.949	1.102	0.668
0.988	1.1198	0.673
1	2.115	0.785

Table 10. Glass Beads measured velocities using the imbibitions technique from Domenico (1977).

Average water saturation (S_w)	Compressional wave velocity V_p (Km/s)	Shear wave velocity V_s (Km/s)
0	1.218	0.774
0.139	1.234	0.730
0.145	1.266	0.726
0.567	1.108	0.728
0.57	1.115	0.736
0.66	1.105	0.647
0.74	1.354	0.714
0.743	1.085	0.647
0.753	1.451	0.673
0.796	1.461	0.691
0.825	1.444	0.687
0.852	1.828	0.654
0.87	2.107	0.714
0.902	1.904	0.654
0.937	1.829	0.658
0.946	2.090	0.704
1	2.071	0.703
1	2.083	0.710
1	2.053	0.772

Table 11. Glass Beads measured velocities using the flow technique.

Two techniques were used to establish partial saturation, the imbibition and flow techniques. The measured velocity values from the imbibition technique are listed in Table 10. The measured velocity data from the flow technique are listed in Table 11.

6.2.2.1 Modeling and interpreting measured and computed ultrasonic velocity models

6.2.2.1.1 Modeling the compressional wave velocities (P-wave)

The data from the imbibition technique was not complete for the whole saturation range, so we provide the missing information from the data of the flow technique. The shear modulus was calculated from the measured shear velocity at the dry point (S_w=0). The results are listed in Table 12. The steps were applied similar to the previous calculations. Some of the parameters and fluid properties of glass beads are listed in Table 13.

Input at $S_w = 0$					Output
ρ_f (g/cm³)	ρ_b (g/cm³)	V_S^2 (km/s)	$\emptyset$	κ	μ (Gpa)
0.132	1.54	0.599	0.383	1	0.895
0.132	1.54	0.599	0.383	1.5	0.905
0.132	1.54	0.599	0.383	2	0.910
0.132	1.54	0.599	0.383	2.5	0.913
0.132	1.54	0.599	0.383	3	0.915
0.132	1.54	0.599	0.383	11	0.922
0.132	1.54	0.599	0.383	∞	0.924

Table 12. Calculations of dynamic shear modulus at different values of mass coupling factor in glass beads at full-gas saturation.

ρ_w (g/cm^3)	ρ_g (g/cm^3)	Ø	C_b (Gpa^{-1})	C_s (Gpa^{-1})	$\beta=C_s/C_b$	$(1-\beta)$
1.13	0.132	0.383	0.95	0.027	0.0285	0.9715

Table13. glass bead parameters and properties used to calculate the effective bulk moduli.

The calculations of the three effective bulk moduli were computed using the same steps mentioned in the Ottawa sand calculations and described in section 6.2.1.1.1. The results are listed in Table 14.

S_w	Reuss K_{sat} (Gpa)	Voigt K_{sat} (Gpa)	Patchy K_{sat} (Gpa)
0	1.074	1.074	1.074
0.05	1.071	2.202	1.155
0.1	1.069	2.884	1.242
0.2	1.067	3.712	1.436
0.4	1.066	4.627	1.937
0.6	1.067	5.221	2.672
0.65	1.068	5.346	2.913
0.7	1.070	5.466	3.187
0.73	1.071	5.536	3.369
0.76	1.072	5.603	3.567
0.8	1.075	5.691	3.859
0.82	1.076	5.734	4.019
0.84	1.079	5.777	4.190
0.86	1.081	5.819	4.372
0.88	1.085	5.860	4.566
0.9	1.090	5.901	4.775
0.92	1.098	5.941	5.000
0.94	1.111	5.981	5.242
0.96	1.137	6.021	5.504
0.98	1.212	6.060	5.789
0.99	1.356	6.079	5.940
0.992	1.425	6.083	5.971
0.994	1.536	6.087	6.002
0.996	1.742	6.091	6.034
0.998	2.262	6.094	6.066
0.999	3.002	6.096	6.082
1	6.098	6.098	6.098

Table 14. Results of calculated effective bulk moduli of uniform, segregated, and patchy saturation distribution in glass beads.

After the effective bulk moduli were computed, the compressional wave velocities were calculated by Biot's high frequency Equation (51). The results of the computed P-wave velocity values are listed in Table 15.

S_w	ρ_f (g/cm^3)	ρ_b (g/cm^3)	$\mu = 0.895$ (Gpa)		
			Reuss V_P (km/s)	Voigt V_P (km/s)	Patchy V_P (km/s)
0	0.132	1.544	1.232	1.232	1.271
0.05	0.182	1.563	1.231	1.508	1.293
0.1	0.232	1.582	1.231	1.652	1.316
0.2	0.332	1.620	1.230	1.812	1.366
0.4	0.531	1.697	1.230	1.974	1.485
0.6	0.731	1.773	1.230	2.073	1.642
0.65	0.781	1.792	1.231	2.093	1.690
0.7	0.831	1.811	1.231	2.112	1.742
0.73	0.861	1.823	1.231	2.123	1.775
0.76	0.890	1.834	1.232	2.134	1.811
0.8	0.930	1.849	1.232	2.147	1.862
0.82	0.950	1.857	1.233	2.154	1.890
0.84	0.970	1.865	1.234	2.161	1.918
0.86	0.990	1.872	1.234	2.167	1.948
0.88	1.010	1.880	1.235	2.173	1.979
0.9	1.030	1.888	1.237	2.180	2.012
0.92	1.050	1.895	1.239	2.186	2.046
0.94	1.070	1.903	1.242	2.192	2.083
0.96	1.090	1.911	1.249	2.198	2.121
0.98	1.110	1.918	1.269	2.204	2.162
0.99	1.120	1.922	1.307	2.207	2.183
0.992	1.122	1.923	1.324	2.207	2.187
0.994	1.124	1.924	1.352	2.208	2.191
0.996	1.126	1.924	1.402	2.209	2.196
0.998	1.128	1.925	1.521	2.209	2.200
0.999	1.129	1.926	1.676	2.210	2.202
1	1.130	1.926	2.210	2.210	2.205

Table 15. Results of computed P-wave velocities versus saturation of the uniform, segregated, and simple patchy models in glass beads.

The computed and measured compressional wave velocities as a function of water saturation are modeled. Figure 21, shows the glass beads velocity curves versus water

saturation of both measured and computed compressional wave velocities at a coupling

factor of one ($\kappa = 1$), and connected-to-total porosity ratio of one.

Figure (21): Results of P-wave velocity models in glass beads as a function of water saturation from Domenico (1977) at coupling factor of one ($\kappa=1$), porosity ratio of one ($\phi_c / \phi_T = 1$), and deferential pressure of 1500 psi.

The flow technique shows heterogeneity in fluid distribution, but most the measured data

did not match the uniform model; also the ending point of the data did not match at the

coupling factor of one. The ending point was able to be matched by varying the coupling

factor value and the ratio of connected-to-total porosity. Figure 22 shows the glass bead

data at a coupling factor of 2.2.
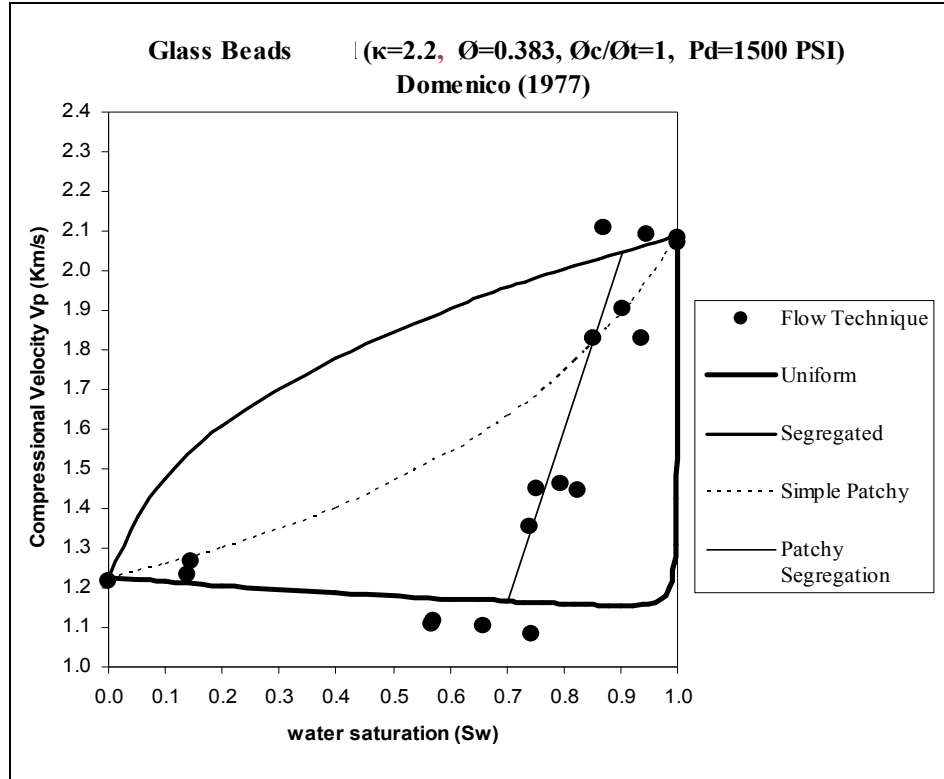
Figure (22) Results of P-wave velocity models in glass beads as a function of water saturation using the flow technique from Domenico (1977) at coupling factor of 2.2 ($\kappa=2.2$), porosity ratio of one ($\phi_c / \phi_T = 1$), and deferential pressure of 1500 psi.

6.2.2.1.2 Interpreting compressional wave velocity models

It is obvious that the flow technique of the fluid injection showed very large scatter of the data at the medium saturation range between $S_w=70\%$ and $S_w=85\%$. The values of measured velocities between $S_w= 55\%$ and $S_w=75\%$ were below the uniform theoretical model, and these values are probably experimental errors, because these four values are below the theoretical model of all coupling factor values. At low water saturation the measured data matched the uniform model, while at medium water-saturation the data fit the patchy segregation model, which is the transitional zone between the uniform and the fully segregated.

70

At very high saturation the data fit the fully segregated model. The patchy segregation

behavior matched many measured values since the permeability is lower than that of

Ottawa sand. The calculation results of the patchy segregation are listed in Table 16.

S_w	$K_{Uniform}$	$K_{Segregated}$	$K_u+4/3\mu$	$K_s+4/3\mu$	ρ_b	$4/3\ \mu$	K_{eff}	V_P
0.7	1.072	5.290	2.265	6.483	1.566	1.193	1.072	1.202
0.93	1.620	5.594	2.813	6.787	1.587	1.193	5.594	1.068

Table 16. Calculations of the patchy segregation model in glass beads.

The transitional zone began at $S_w = 70\%$ to $S_w = 93\%$. The saturation value in the

calculation was taken from 0 at the starting transitional zone (uniform saturation) to 1 at

the ending point (segregated saturation). The flow technique created larger fully

segregated gas patches. The value above the segregated model was also interpreted as an

experimental error. Another fit to the glass bead data can be done by separating the

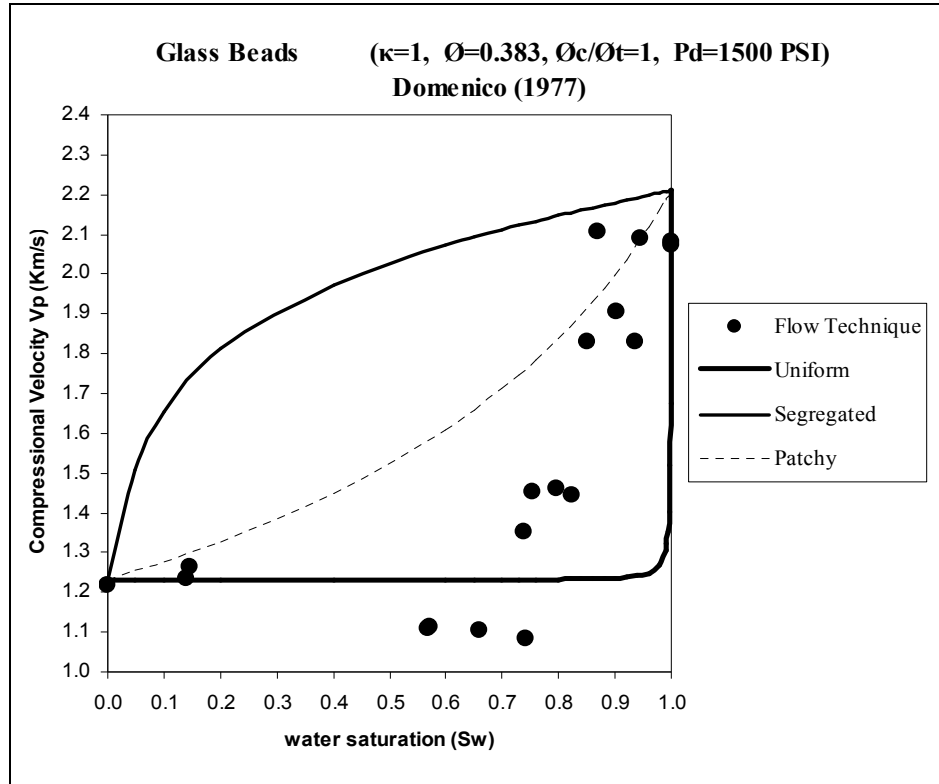porosity at a ratio of connected-to-total of 0.77; Figure 23 shows the results.

71
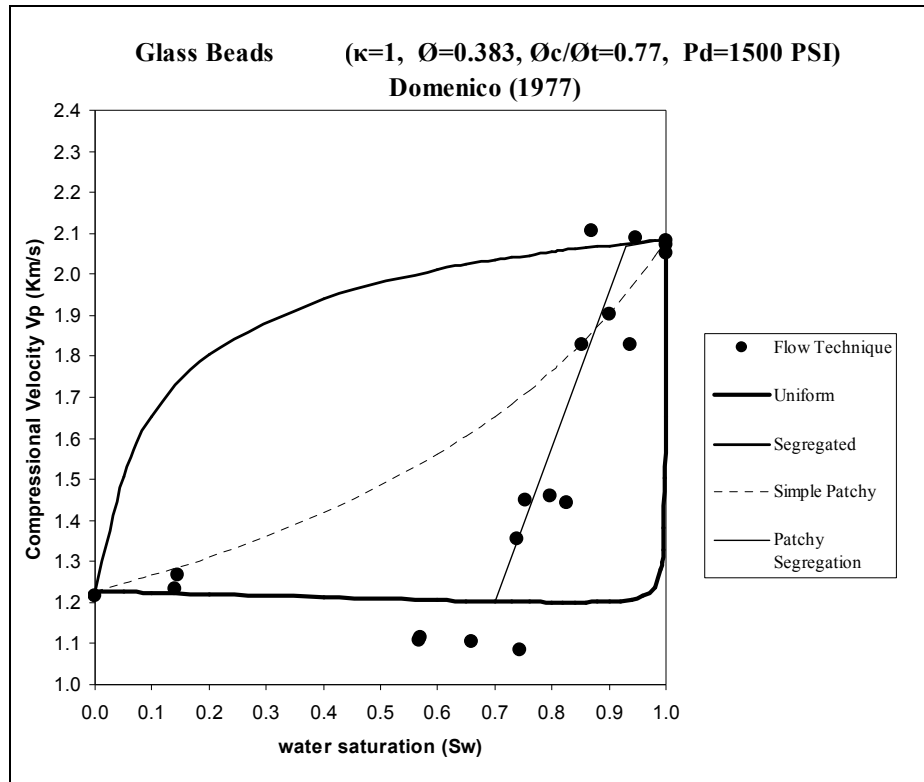
Figure (23): Curve fit of P-wave velocity models in glass beads as a function of water saturation from Domenico (1977) at a differential pressure of 1500 psi. Curve fit parameters include a coupling factor of one, connected-to-total porosity ratio of 0.77. The solid circles are saturations established using the flow technique.

Both methods showed almost similar results in fitting the ending and starting points of the models. The results from the porosity separation are more accurate in fitting the data on the patchy segregation model. The flow technique resulted in a large segregation of the fluid. However, the imbibition technique showed more uniform behavior than the flow technique. The modeling results of compressional wave velocity data of glass bead are shown in Figure (24).
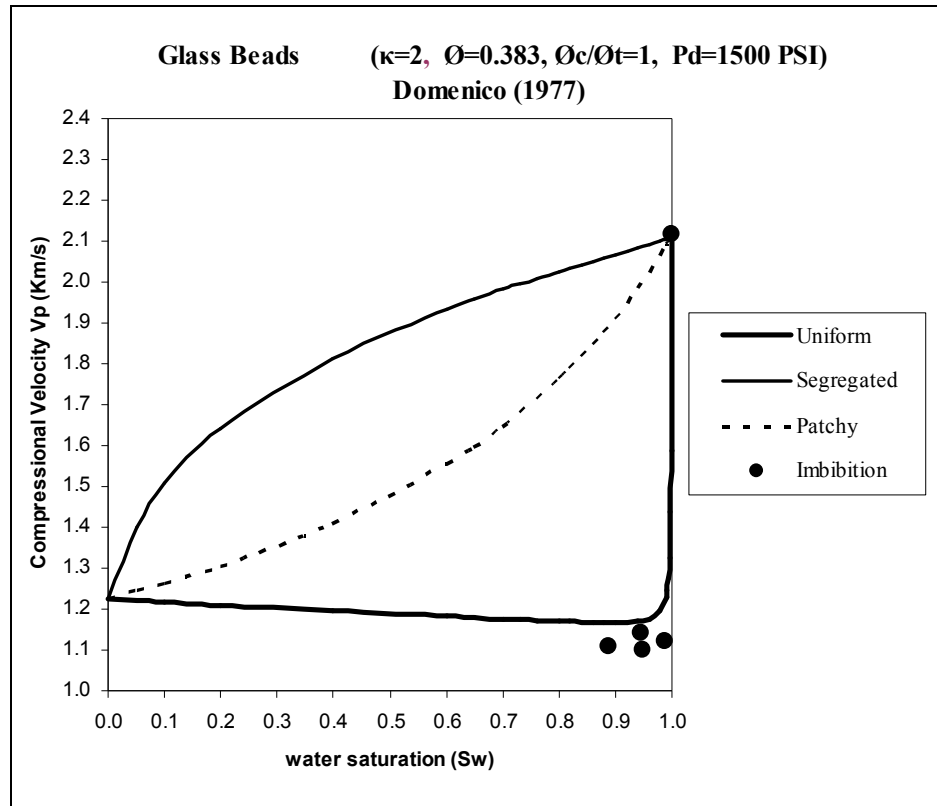
Figure (24): Curve fit of P-wave velocity models in glass beads as a function of water saturation from Domenico (1977) at a differential pressure of 1500 psi. Curve fit parameters include coupling factor of 2, connected to total porosity ratio of 1.The Solid circles are saturations established using the imbibition technique.

The imbibition technique resulted in more uniform distribution. The measured data was quite near the uniform model at a coupling factor κ = 2. The measured data using the imbibition technique were not complete for the whole saturation range, so the same input data of the flow technique were used in modeling the data. Because the data were complete, there were three measured values under the uniform theoretical model. The exact value of mass coupling factor was not known through the measurements, so varying the value resulted in good agreement between measured and computed P-wave velocities.

6.2.2.1.3 Modeling the shear-wave velocities (S-wave)

The calculated shear-wave velocities are listed versus water saturation at different values of mass coupling factor (κ =1, 1.5,3, and ∞) were modeled, and Table (17) shows the results.

S_w	ρ_f (g/cm³)	ρ_b (g/cm³)	$\kappa = 1$ μ=0.895 (Gpa) V_S (km/s)	$\kappa = 1.5$ μ=0.905 (Gpa) V_S (km/s)	$\kappa = 3$ μ= 0.915 (Gpa) V_S (km/s)	$\kappa = \infty$ μ= 0.924 (Gpa) V_S (km/s)
0	0.132	1.544	0.770	0.771	0.773	0.774
0.05	0.182	1.563	0.774	0.773	0.771	0.769
0.1	0.232	1.582	0.774	0.771	0.768	0.765
0.2	0.332	1.620	0.774	0.768	0.762	0.756
0.4	0.531	1.697	0.774	0.761	0.750	0.739
0.6	0.731	1.773	0.774	0.755	0.738	0.723
0.65	0.781	1.792	0.774	0.754	0.735	0.719
0.7	0.831	1.811	0.774	0.752	0.733	0.716
0.73	0.861	1.823	0.774	0.751	0.731	0.713
0.76	0.890	1.834	0.774	0.750	0.729	0.711
0.8	0.930	1.849	0.774	0.749	0.727	0.708
0.82	0.950	1.857	0.774	0.749	0.726	0.707
0.84	0.970	1.865	0.774	0.748	0.725	0.705
0.86	0.990	1.872	0.774	0.748	0.724	0.704
0.88	1.010	1.880	0.774	0.747	0.723	0.702
0.9	1.030	1.888	0.774	0.746	0.722	0.701
0.92	1.050	1.895	0.774	0.746	0.721	0.700
0.94	1.070	1.903	0.774	0.745	0.720	0.698
0.96	1.090	1.911	0.774	0.745	0.719	0.697
0.98	1.110	1.918	0.774	0.744	0.718	0.696
0.99	1.120	1.922	0.774	0.744	0.717	0.695
0.992	1.122	1.923	0.774	0.744	0.717	0.695
0.994	1.124	1.924	0.774	0.744	0.717	0.695
0.996	1.126	1.924	0.774	0.744	0.717	0.694
0.998	1.128	1.925	0.774	0.743	0.717	0.694
0.999	1.129	1.926	0.774	0.743	0.773	0.694
1	1.130	1.926	0.774	0.743	0.771	0.694

Table 17. Results of computed S-wave velocities versus saturation in glass beads at different coupling factor values.

The shear-wave velocities modeled versus saturation with the measured data of the flow and imbibition techniques are shown in Figure (25).
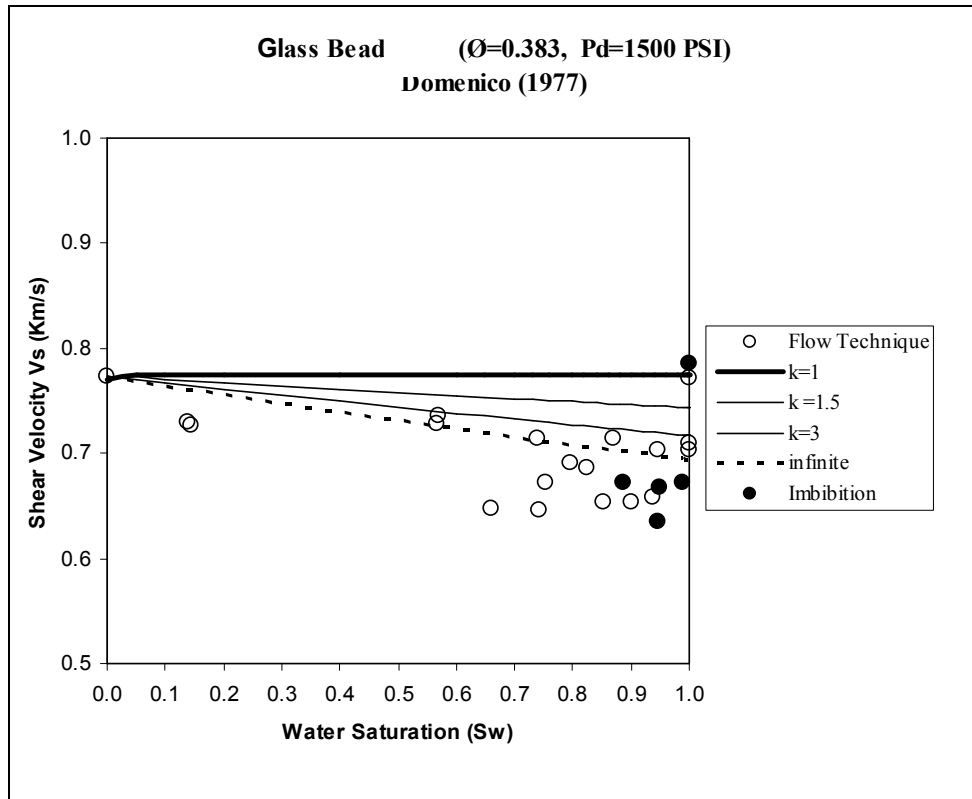
Figure (25): Curve fit of S-wave velocity in glass beads as a function of water saturation from Domenico (1977) at a coupling factor of (κ=1, 1.5, 3, ∞) and pressure of 1500 psi. Solid circles are saturations established using an imbibition technique, and open circles are for a flow technique.

6.2.2.1.4 Interpreting shear-wave velocity models (S-wave)

Measured shear-wave velocities were near the theoretical curve for $\kappa = 3$, and some of the data were below the theoretical curve for $\kappa = \infty$. The starting and ending points agreed with the theoretical curve for $\kappa = 1$. In general, shear-wave velocity decreased with increasing water saturation. The difference in data values versus saturation between the Ottawa sands and glass beads is related to the difference in pore shape and grain size. So the dynamic motion of the fluid is different. In the flow technique, the gas is distributed inside round pores (stiff pores) as water saturation increases, and a mix of patches of uniform and segregated gas distribution are formed.

75

The non-uniformity in gas distribution gives the higher velocities that fit the patchy segregation model.

6.3 Medium-porosity rocks, consolidated sandstone (Boise sandstone)

Gregory (1976) measured ultrasonic compressional and shear-wave velocities in partially saturated consolidated sandstones. The water saturation was reduced by the evaporation of water, and the air saturation was increased.

6.3.1. Boise sandstone

Boise sandstone is Pliocene in age, and has a porosity of 26.80 %, ($\phi = 0.268$). It is an arkose, consisting of quartz and chert, 60 %; feldspar, 40%; mica, trace; rock fragments, trace, clay, trace. The silica is cemented, and the sand is moderately sorted. The ultrasonic velocities were measured at 1000 kHz frequency, and at pressure of 1000, 5000 psi. Saturation was established by the drying technique. The measured data are listed in Table (18).

Water saturation percent (S_w)	Compressional wave velocity V_p (Km/s)	Shear wave velocity V_s (Km/s)
0.0	3.087	1.999
5.0	3.089	2.046
10.0	3.078	2.051
20.0	3.078	2.020
40.0	3.078	2.016
60.0	3.246	2.010
80.0	3.360	1.994
100.0	3.401	1.959

Table 18. Measured compressional and shear-wave velocity values versus saturation in Boise sandstone from Gregory (1976).

6.3.1.1 Modeling and interpreting measured and computed ultrasonic velocity models

6.3.1.1.1 Modeling the compressional wave velocity (P-wave)

The dynamic shear modulus (μ) was calculated from the measured shear velocity at full-gas saturation by Equation (50). The shear modulus was assumed to be independent of saturation. The dry and the wetted shear moduli were equal ($\mu_{Dry} = \mu_{wet}$). The shear modulus varied with the coupling factor (κ). The input and output parameters are listed in Table 19. The value of gas density was different at pressure (1000 psi). The fluid density (ρ_f) was computed from Equation (9), and the bulk density (ρ_b) was computed from Equation (8).

Input at $S_w = 0$					Output
ρ_f (g/cm³)	ρ_b (g/cm³)	V^2_s (km/s)	$\varnothing$	κ	μ (Gpa)
0.088	1.66	3.996	0.268	1	7.751
0.088	1.66	3.996	0.268	1.5	7.783
0.088	1.66	3.996	0.268	2	7.799
0.088	1.66	3.996	0.268	2.5	7.808
0.088	1.66	3.996	0.268	3	7.814
0.088	1.66	3.996	0.268	11	7.837
0.088	1.66	3.996	0.268	∞	7.845

Table 19. Calculations of dynamic shear modulus at different values of mass coupling factor in Boise sandstone at full gas saturation from Gregory (1967).

After the shear modulus is determined, the calculation of the effective bulk modulus (K_{sat}) began. From Equation (48), the input parameters were calculated starting with the frame compressibility (C_b) which is computed from the measured compressional and shear velocities by Equation (49).

The rock bulk density increased with water saturation since the density of water is higher than gas. Some input parameters are listed in Table (20).

ρ_w (g/cm^3)	ρ_g (g/cm^3)	$\O_T$	C_b (Gpa^{-1})	C_s (Gpa^{-1})	$\beta = C_s/C_b$	$(1-\beta)$
1.0	0.088	0.268	0.121	0.027	0.22	0.78

Table 20. Boise sandstone parameters used to calculate the effective bulk moduli.

The calculations of the three effective bulk moduli were computed using the same steps described in section 6.2.1.1.1. The results are listed in Table 21.

S_w	Reuss K_{sat} (Gpa)	Voigt K_{sat} (Gpa)	Patchy K_{sat} (Gpa)
0	8.263	8.263	8.263
0.05	8.262	9.975	8.487
0.1	8.262	10.855	8.717
0.2	8.261	11.803	9.193
0.4	8.261	12.733	10.221
0.6	8.261	13.290	11.364
0.65	8.262	13.405	11.670
0.7	8.262	13.514	11.984
0.73	8.262	13.577	12.177
0.76	8.262	13.638	12.373
0.8	8.262	13.717	12.641
0.82	8.263	13.755	12.777
0.84	8.263	13.793	12.914
0.86	8.263	13.830	13.053
0.88	8.264	13.867	13.194
0.9	8.264	13.903	13.337
0.92	8.265	13.939	13.481
0.94	8.267	13.974	13.628
0.96	8.271	14.009	13.776
0.98	8.281	14.043	13.925
0.99	8.301	14.061	14.001
0.992	8.312	14.064	14.016
0.994	8.329	14.067	14.031
0.996	8.362	14.071	14.047
0.998	8.460	14.074	14.062
0.999	8.647	14.076	14.069
1	14.077	14.077	14.077

Table 21. Results of calculated effective bulk moduli of uniform, segregated, and patchy saturation models in Boise sandstone at $\kappa=1$ and connected-to-total porosity ratio of one, from Gregory (1976).

Then the P-wave velocities of the three models were calculated from Equation (49), and the compressional wave velocity results of the three different distribution models are listed in Table (22).

| S_w | ρ_f (g/cm^3) | ρ_b (g/cm^3) | μ= 7.751 (Gpa) | | |
			Reuss V_P (km/s)	Voigt V_P (km/s)	Patchy V_P (km/s)
0	0.088	1.963	3.096	3.096	3.096
0.05	0.134	1.976	3.096	3.236	3.115
0.1	0.179	1.988	3.096	3.305	3.134
0.2	0.270	2.012	3.096	3.378	3.173
0.4	0.453	2.061	3.096	3.448	3.255
0.6	0.635	2.110	3.096	3.490	3.345
0.65	0.681	2.122	3.096	3.498	3.368
0.7	0.726	2.134	3.096	3.506	3.392
0.73	0.754	2.142	3.096	3.511	3.407
0.76	0.781	2.149	3.096	3.515	3.421
0.8	0.818	2.159	3.096	3.521	3.442
0.82	0.836	2.164	3.096	3.524	3.452
0.84	0.854	2.169	3.096	3.527	3.462
0.86	0.872	2.174	3.096	3.529	3.472
0.88	0.891	2.178	3.096	3.532	3.483
0.9	0.909	2.183	3.096	3.535	3.493
0.92	0.927	2.188	3.097	3.537	3.504
0.94	0.945	2.193	3.097	3.540	3.515
0.96	0.964	2.198	3.097	3.543	3.526
0.98	0.982	2.203	3.098	3.545	3.536
0.99	0.991	2.205	3.100	3.546	3.542
0.992	0.993	2.206	3.100	3.547	3.543
0.994	0.995	2.206	3.102	3.547	3.544
0.996	0.996	2.207	3.105	3.547	3.545
0.998	0.998	2.207	3.113	3.547	3.546
0.999	0.999	2.208	3.128	3.547	3.547
1	1.000	2.208	3.548	3.548	3.547

Table 22. Results of computed P-wave velocities versus saturation of the uniform, segregated, and simple patchy models in Boise sandstone.

Figure 26 shows the Boise sandstone velocity curves versus water saturation of both measured and computed compressional wave velocities at a coupling factor of one (κ =1), and a connected-to-total porosity ratio of one.

Figure (26) Results of P-wave velocity models in Boise sandstone as a function of water saturation from Gregory (1976) at a coupling factor of one (κ=1), porosity ratio of one (ϕ_c / ϕ_T =1), and deferential pressure of 1000 psi.

At low saturation the measured value were near the theoretical model of uniform distribution, but at saturation higher than 50%, the measured data were not consistent with the theoretical models, and the ending point did not match.

The ending point was able to fit the theoretical models when the porosity is separated at a ratio of connected-to-total of 0.89, which means that 11% of the total porosity was disconnected. The fit also occurred at a mass coupling factor of 1.5. Many values of the porosity ratio and coupling were tested until the best fit occurred. The results of fitting the measured P-wave velocities with the theoretical models are shown in Figure (27). The calculations of the patchy segregation model are listed in Table 23.

S_w	$K_{Uniform}$	$K_{Segregated}$	$K_u+4/3\mu$	$K_s+4/3\mu$	ρ_b	$4/3\,\mu$	K_{ef}	V_P
0.4	8.261	11.779	18.648	22.166	1.959	10.387	8.261	3.085
0.8	8.262	12.894	18.649	23.281	2.049	10.387	12.894	3.371

Table 23. Calculations of the patchy segregation model in Boise sandstone.

Figure (27): Curve fit of P-wave velocity models in Boise sandstone as a function of water saturation from Gregory (1976) at a differential pressure of 1000 psi. Curve fit parameters include a coupling factor of κ =1.5, connected-to-total porosity ratio of 0.89, and a patchy segregation model from S_w = 40% to S_w = 100%. Solid circles are saturations established using the drying technique.

6.3.1.1.2 Interpreting compressional wave-velocity models

The data could be interpreted after the ending point was matched at full-water saturation. The measured data fit the uniform theoretical model at low-water saturation. With increasing saturation at S_w= 40% the measured velocity increased to fit the transitional patchy segregation model. Then with increasing water saturation the measured data still fit the patchy segregation model, which fell between the simple

81

patchy and fully segregated models. The saturation curve in Boise sandstone exhibited two saturation regimes: the uniform at low saturation, and the patchy segregation at medium and high water saturation. The two saturation regimes produced in Boise sandstone are related to the medium porosity and permeability.

6.3.1.1.3 Modeling the shear-wave velocities (S-wave)

The calculated shear wave velocities are listed in Table 24.

S_w	ρ_f (g/cm^3)	ρ_b (g/cm^3)	$\kappa = 1$ $\mu=7.751$ (Gpa) V_S (km/s)	$\kappa = 1.5$ $\mu=7.783$ (Gpa) V_S (km/s)	$\kappa = 3$ $\mu= 7.814$ (Gpa) V_S (km/s)	$\kappa = \infty$ $\mu= 7.845$ (Gpa) V_S (km/s)
0	0.088	1.963	1.999	1.999	1.999	1.999
0.05	0.134	1.976	1.999	1.997	1.995	1.993
0.1	0.179	1.988	1.999	1.995	1.991	1.987
0.2	0.270	2.012	1.999	1.991	1.983	1.975
0.4	0.453	2.061	1.999	1.983	1.966	1.952
0.6	0.635	2.110	1.999	1.974	1.951	1.930
0.65	0.681	2.122	1.999	1.972	1.947	1.924
0.7	0.726	2.134	1.999	1.970	1.943	1.919
0.73	0.754	2.142	1.999	1.969	1.941	1.916
0.76	0.781	2.149	1.999	1.968	1.939	1.912
0.8	0.818	2.159	1.999	1.966	1.935	1.908
0.82	0.836	2.164	1.999	1.966	1.934	1.906
0.84	0.854	2.169	1.999	1.965	1.932	1.904
0.86	0.872	2.174	1.999	1.964	1.931	1.902
0.88	0.891	2.178	1.999	1.963	1.929	1.900
0.9	0.909	2.183	1.999	1.962	1.928	1.898
0.92	0.927	2.188	1.999	1.962	1.926	1.896
0.94	0.945	2.193	1.999	1.961	1.925	1.894
0.96	0.964	2.198	1.999	1.960	1.924	1.891
0.98	0.982	2.203	1.999	1.959	1.922	1.889
0.99	0.991	2.205	1.999	1.959	1.921	1.888
0.992	0.993	2.206	1.999	1.959	1.921	1.888
0.994	0.995	2.206	1.999	1.959	1.921	1.888
0.996	0.996	2.207	1.999	1.959	1.921	1.888
0.998	0.998	2.207	1.999	1.959	1.921	1.888
0.999	0.999	2.208	1.999	1.959	1.921	1.887
1	1.000	2.208	1.999	1.958	1.921	1.887

Table 24. Results of computed S-wave velocities versus saturation in Boise sandstone at different coupling factor values.

The measured and computed shear-wave velocities versus water saturation were modeled as shown in Figure (28).

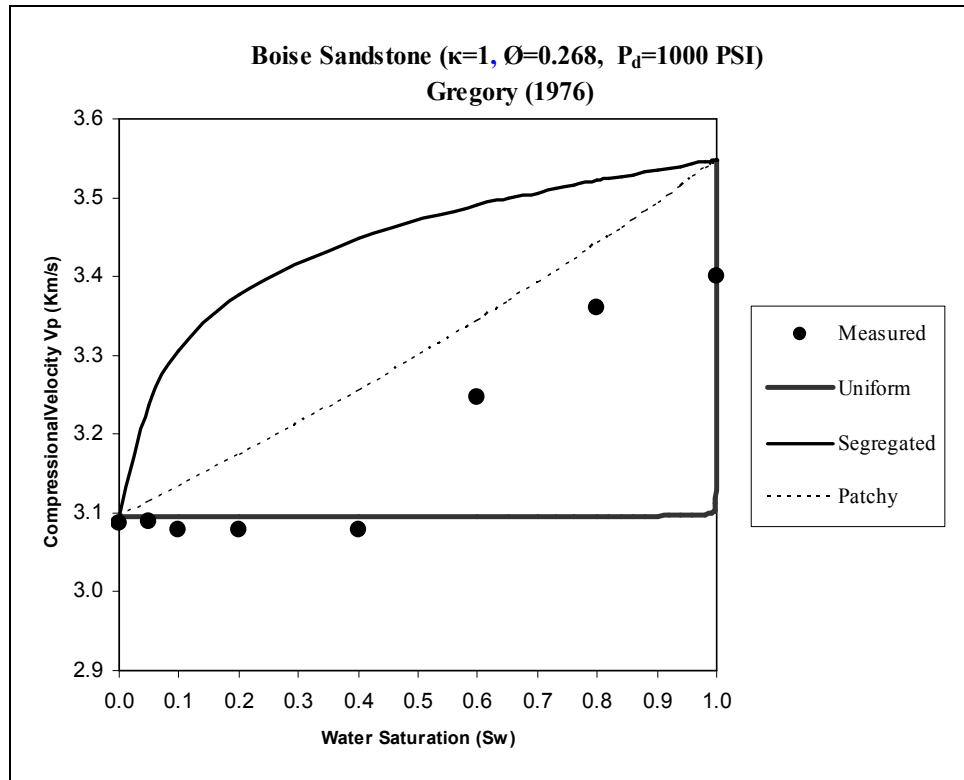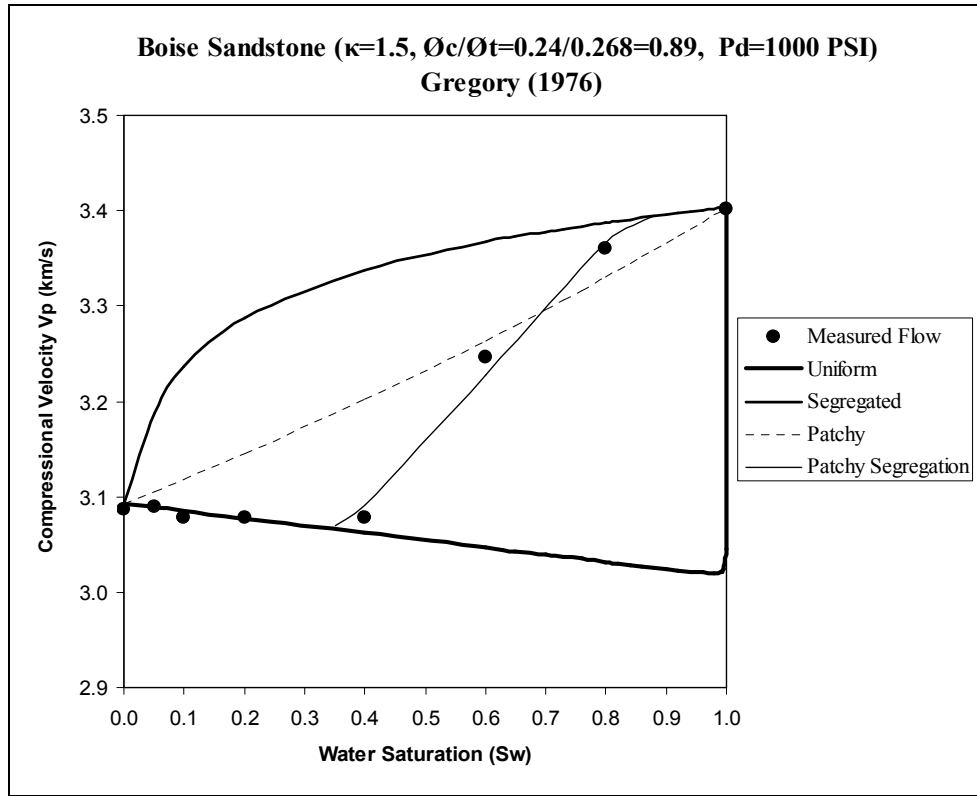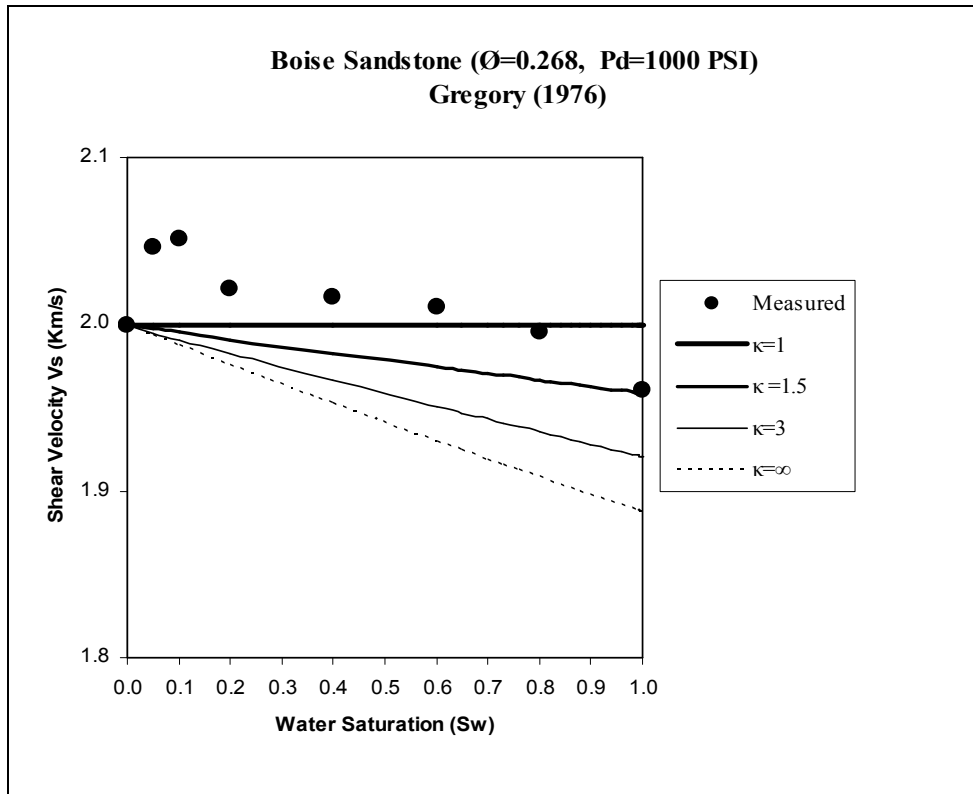Figure 28: Curve fit of S-wave velocity in Boise sandstone as a function of water saturation from Gregory (1976) at a coupling factor of (κ=1, 1.5, 3, ∞) and pressure of 1000 psi. Solid circles are saturations established using a flow technique.

6.3.1.1.4 Interpreting shear-wave velocity models (S-wave)

The measured shear-wave velocity was higher than that of the theoretical models at medium-water saturation. The starting and ending points fit exactly the theoretical model at a coupling factor of value equal to 1.5. The shear wave velocity decreased linearly after S_w=20%. The measured shear-wave velocity was near the theoretical models at a coupling factor between 1 and 1.5.

6.4   Low-porosity rocks

6.4.1   Tight gas sand

Knight and Nolen-Hoeksema (1991) measured the ultrasonic velocities at 1000 kHz frequency in tight gas sand from the Spirit River Formation in the Alberta Basin. The sample has low porosity ($\phi = 0.052$) and a permeability of 1 micro-darcy. The pores are poorly connected by very narrow capillaries causing very low permeability. The saturation was established through the imbibition and drainage techniques. The water saturation was increased by the imbibition method (injecting water) while the air saturation was increased through the drainage method (water evaporation).

The experiment started by measuring the dry sample at $S_w = 0$ % and going through a maximum saturation of $S_w = 90\%$. The velocity measurements were made under no pressure effect. The data measured during the drainage technique are listed in Table 25; the data is taken from Gist (1994). Figure 29 shows a thin section of tight gas sandstone.
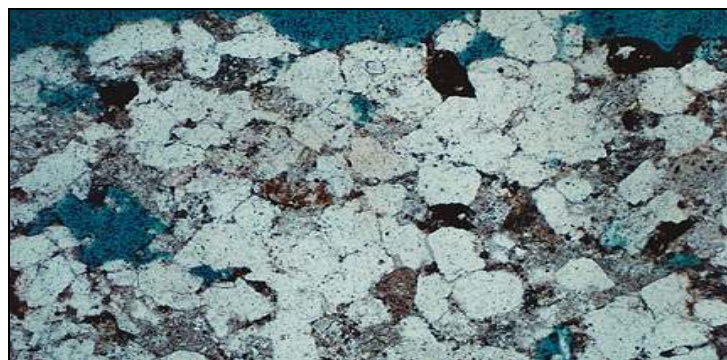
Taken from energy.usgs.gov/.../Petroleum/section2.jpeg

Figure (29): Photo of Tight Gas Sandstone.

Average water saturation (S_w)	Compressional wave velocity V_P (Km/s)	Shear wave velocity V_S (Km/s)
0	2.980	2.19
0.11	2.960	2.2
0.13	2.960	2.17
0.14	2.960	2.17
0.16	2.937	2.16
0.18	2.960	2.15
0.2	2.960	2.17
0.22	2.937	2.15
0.25	2.921	2.13
0.29	2.937	2.13
0.31	2.937	2.12
0.32	2.971	2.12
0.37	2.948	2.14
0.39	2.960	2.12
0.43	2.990	2.15
0.45	3.029	2.2
0.46	3.033	2.2
0.49	3.052	2.175
0.51	3.029	2.17
0.53	3.121	2.2
0.55	3.167	2.21
0.57	3.229	2.2
0.6	3.282	2.24
0.62	3.328	2.29
0.63	3.397	2.285
0.65	3.454	2.285
0.67	3.534	2.335
0.69	3.695	2.35
0.71	3.695	2.375
0.72	3.741	2.4
0.75	3.849	2.375
0.76	3.879	2.4
0.79	3.909	2.425
0.8	4.001	2.425
0.83	4.086	2.44
0.85	4.121	2.425
0.88	4.144	2.45
0.9	4.144	2.42

Table 25. Measured P-wave and S-wave velocity values versus water saturation during the drainage technique in Spirit River Tight Gas Sand.

6.4.1.1 Modeling and interpreting measured and computed ultrasonic velocity models

6.4.1.1.1 Modeling the compressional wave velocities (P-wave)

The dynamic shear modulus (μ) is calculated from the measured shear velocity at full-gas saturation by Equation (50). The shear modulus varies with the coupling factor (κ). The input and output parameters are listed in Table 26. The value of air density is different at pressure 1 psi. The dynamic shear modulus (μ) did not changing with coupling factor.

Input at $S_w= 0$					Output
ρ_f (g/cm³)	ρ_b (g/cm³)	V^2_s (km/s)	$\varnothing$	κ	μ (Gpa)
0.000088	2.512	4.796	0.052	1	12.05
0.000088	2.512	4.796	0.052	1.5	12.05
0.000088	2.512	4.796	0.052	2	12.05
0.000088	2.512	4.796	0.052	2.5	12.05
0.000088	2.512	4.796	0.052	3	12.05
0.000088	2.512	4.796	0.052	11	12.05
0.000088	2.512	4.796	0.052	∞	12.05

Table 26. Calculations of dynamic shear modulus at different values of mass coupling factor in tight gas sand at full gas saturation from Knight and Nolen-Hoeksema (1990).

The very low porosity was the reason for the shear modulus not changing. After the shear modulus was determined, the calculation of the effective bulk moduli (K_{sat}) began. From Equation (48), the input parameters were calculated starting with frame compressibility (C_b) which was computed from the measured compressional and shear velocities by Equation (49). The rock bulk density increased with water saturation since the density of

water is higher than gas. Some input parameters are listed in Table 27. The air compressibility was very high under no atmospheric pressure.

ρ_w (g/cm³)	ρ_g (g/cm³)	$\emptyset_T$	C_b (Gpa⁻¹)	C_s (Gpa⁻¹)	$\beta=C_s/C_b$	(1-β)
1.0	0.000088	0.052	0.16	0.027	0.17	0.83

Table 27. Tight gas sand parameters used to calculate the effective bulk moduli.

The results of effective bulk moduli are listed in Table (28).

S_w	Reuss K_{sat} (Gpa)	Voigt K_{sat} (Gpa)	Simple Patchy K_{sat} (Gpa)
0	6.279	6.279	6.279
0.05	6.250	14.142	6.847
0.1	6.250	16.061	7.445
0.2	6.250	19.042	8.740
0.4	6.250	22.958	11.813
0.6	6.250	25.416	15.758
0.65	6.250	25.894	16.925
0.7	6.250	26.331	18.182
0.73	6.250	26.576	18.983
0.76	6.250	26.809	19.822
0.8	6.250	27.103	21.006
0.82	6.250	27.243	21.628
0.84	6.250	27.378	22.271
0.86	6.250	27.510	22.936
0.88	6.250	27.638	23.625
0.9	6.250	27.762	24.339
0.92	6.250	27.883	25.079
0.94	6.251	28.000	25.847
0.96	6.251	28.114	26.644
0.98	6.252	28.224	27.471
0.99	6.253	28.279	27.897
0.992	6.254	28.289	27.984
0.994	6.255	28.300	28.070
0.996	6.258	28.311	28.157
0.998	6.265	28.321	28.244
0.999	6.281	28.327	28.288
1	28.332	28.332	28.332

Table 28. Results of calculated effective bulk moduli of uniform, segregated, and patchy saturation models in gas tight sand at κ=1 and connected-to-total porosity ratio of one, from Knight and Nolen-Hoeksema (1990).

The compressional wave velocity results of the three different distribution models are listed in Table 29.

S_w	ρ_f (g/cm^3)	ρ_b (g/cm^3)	Reuss V_P (km/s)	Voigt V_P (km/s)	Simple Patchy V_P (km/s)
			$\mu = 12$ (Gpa)		
0	0.000088	2.512	2.978	2.978	2.978
0.05	0.050084	2.515	2.975	3.463	3.015
0.1	0.100079	2.517	2.974	3.570	3.053
0.2	0.200070	2.523	2.973	3.731	3.135
0.4	0.400053	2.533	2.969	3.929	3.320
0.6	0.600035	2.543	2.966	4.046	3.543
0.65	0.650031	2.546	2.965	4.068	3.607
0.7	0.700026	2.549	2.964	4.088	3.674
0.73	0.730024	2.550	2.964	4.100	3.716
0.76	0.760021	2.552	2.963	4.110	3.760
0.8	0.800018	2.554	2.962	4.123	3.820
0.82	0.820016	2.555	2.962	4.129	3.852
0.84	0.840014	2.556	2.962	4.135	3.884
0.86	0.860012	2.557	2.961	4.141	3.917
0.88	0.880011	2.558	2.961	4.147	3.952
0.9	0.900009	2.559	2.961	4.152	3.986
0.92	0.920007	2.560	2.960	4.157	4.022
0.94	0.940005	2.561	2.960	4.163	4.059
0.96	0.960004	2.562	2.960	4.167	4.097
0.98	0.980002	2.563	2.959	4.172	4.136
0.99	0.990001	2.564	2.959	4.174	4.156
0.992	0.992001	2.564	2.959	4.175	4.161
0.994	0.994001	2.564	2.959	4.175	4.165
0.996	0.996000	2.564	2.960	4.176	4.169
0.998	0.998000	2.564	2.960	4.176	4.173
0.999	0.999000	2.564	2.961	4.177	4.175
1	1.000000	2.564	4.177	4.177	4.177

Table 29. Results of computed P-wave velocities versus saturation of the uniform, segregated, and simple patchy models in tight gas sand.

Figure 30 shows Alberta gas tight sand velocity curves versus water saturation of both measured and computed compressional wave velocities at a coupling factor of one ($\kappa = 1$), and connected-to-total porosity ratio of one.

Figure 30: Results of P-wave velocity models in Alberta Gas Tight Sand as a function of water saturation from Knight and Nolen-Hoeksema (1990) at coupling factor of one (κ=1), porosity ratio of one (ϕ_c / ϕ_T =1).

Because the porosity was very low, some error in separating the total porosity could have given wrong results. As seen in Figure (30), the measured P-wave velocities matched the theoretical model of the uniform distribution at saturations between S_w = 0 % and S_w = 45%. The ending point did not match the theoretical models. The ending point was able to be matched if the porosity decreased to a value of 0.023.

We consider there was an error in measuring the porosity in the laboratory experiment. The results of reducing the porosity are shown in Figure 31. The patchy segregation model calculations are listed in Table 30.

S_w	S_w	K_{uni}	K_{seg}	$4/3\ \mu$	$K_{uni}+4/3\ \mu$	$K_{seg}+4/3\ \mu$	K_{eff}	V_P	ρ_b
0.00	0.42	6.25	23.57	16.00	22.25	39.57	6.25	2.97	2.52
0.14	0.48	6.25	24.19	16.00	22.25	40.19	7.77	3.07	2.53
0.29	0.53	6.25	24.80	16.00	22.25	40.80	9.58	3.18	2.53
0.43	0.59	6.25	25.66	16.00	22.25	41.66	11.81	3.32	2.53
0.57	0.65	6.25	26.11	16.00	22.25	42.11	14.47	3.47	2.53
0.72	0.71	6.25	26.58	16.00	22.25	42.58	17.78	3.65	2.53
0.86	0.76	6.25	26.96	16.00	22.25	42.96	21.94	3.87	2.53
1.00	0.82	6.25	27.44	16.00	22.25	43.44	27.49	4.14	2.54

Table 30. Calculations of the patchy segregation model in tight gas sand.

The transitional patchy segregation zone started from ($S_w = 0.42$) and ended at ($S_w = 0.82$). The values between the starting and ending points were interpolated as listed in Table 30. The result of the patchy segregation model is shown in Figure 31.

6.4.1.1.2 Interpreting compressional wave velocity models

The Spirit Tight Gas Sand measured data fit the uniform model at low-water saturation and the patchy segregation at medium-water saturation, and finally the data fit the fully segregated model at high-water saturation. The patchy segregation fit most of the data. Because the porosity and permeability was very low the fluid distribution was quite segregated non-uniformly. The gas probably filled the high aspect ratio pores, while the wetting fluid (water) filled the low aspect ratio pores with increasing water saturation until the data fit the segregated model at high water saturation, where the water filled the pores of high aspect ratio completely, which made the rock stiffer and that led to higher velocities.
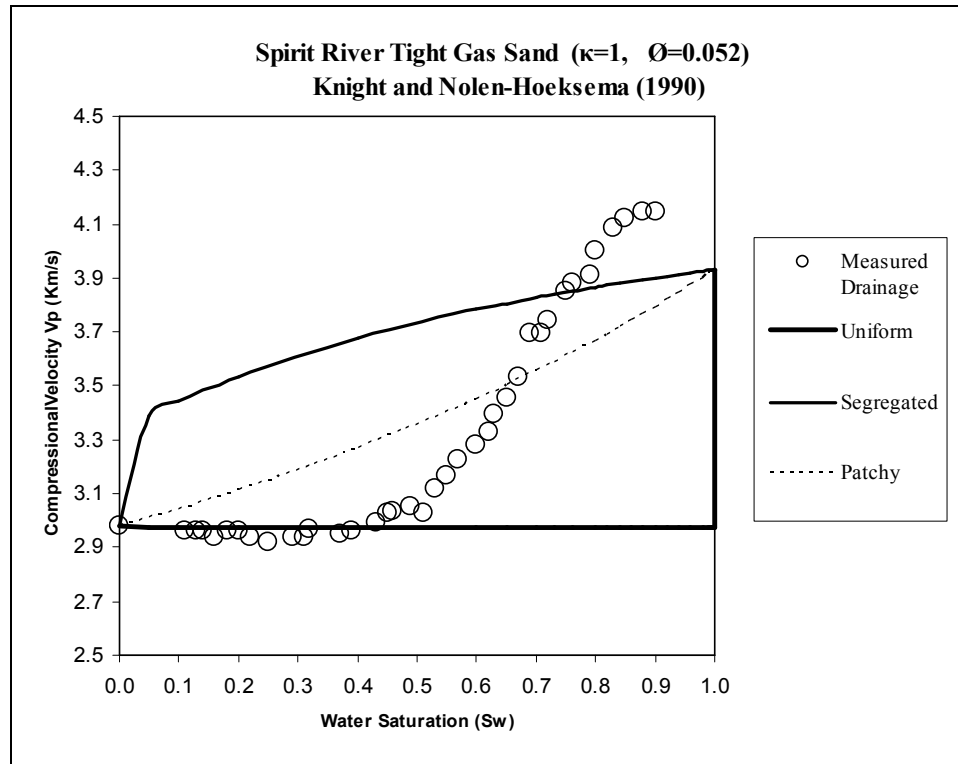
Figure (31): Curve fit of P-wave velocity models in Alberta Tight Gas Sand as a function of water saturation from Knight and Nolen-Hoeksema (1990). Curve fit parameters include coupling factor of $\kappa = 1$, connected porosity = 0.023, and a patchy segregation model from S_w=42% to S_w= 82%. Solid circles are saturations established using the drying technique.

6.4.1.1.3 Modeling the shear-wave velocities (S-wave)

The calculated shear-wave velocity were listed versus water saturation at different values of mass coupling factors ($\kappa = 1$, and ∞), and Table (31) shows the results. The data were measured during the drainage cycle. The measured and calculated shear-wave velocities were modeled versus water saturation as shown in Figure (32).

S_w	ρ_f (g/cm^3)	ρ_b (g/cm^3)	$\kappa = 1$ $\mu=12$ (Gpa) V_S (km/s)	$\kappa = 1.5$ $\mu=12$ (Gpa) V_S (km/s)	$\kappa = 3$ $\mu= 12$ (Gpa) V_S (km/s)	$\kappa = \infty$ $\mu= 12$ (Gpa) V_S (km/s)
0	0.000088	2.512	2.186	2.186	2.186	2.186
0.05	0.050084	2.515	2.186	2.185	2.185	2.184
0.1	0.100079	2.517	2.186	2.185	2.184	2.183
0.2	0.200070	2.523	2.186	2.184	2.183	2.181
0.4	0.400053	2.533	2.186	2.183	2.180	2.177
0.6	0.600035	2.543	2.186	2.181	2.177	2.172
0.65	0.650031	2.546	2.186	2.181	2.176	2.171
0.7	0.700026	2.549	2.186	2.180	2.175	2.170
0.73	0.730024	2.550	2.186	2.180	2.175	2.170
0.76	0.760021	2.552	2.186	2.180	2.174	2.169
0.8	0.800018	2.554	2.186	2.180	2.174	2.168
0.82	0.820016	2.555	2.186	2.179	2.173	2.168
0.84	0.840014	2.556	2.186	2.179	2.173	2.167
0.86	0.860012	2.557	2.186	2.179	2.173	2.167
0.88	0.880011	2.558	2.186	2.179	2.172	2.166
0.9	0.900009	2.559	2.186	2.179	2.172	2.166
0.92	0.920007	2.560	2.186	2.179	2.172	2.165
0.94	0.940005	2.561	2.186	2.179	2.172	2.165
0.96	0.960004	2.562	2.186	2.178	2.171	2.165
0.98	0.980002	2.563	2.186	2.178	2.171	2.164
0.99	0.990001	2.564	2.186	2.178	2.171	2.164
0.992	0.992001	2.564	2.186	2.178	2.171	2.164
0.994	0.994001	2.564	2.186	2.178	2.171	2.164
0.996	0.996000	2.564	2.186	2.178	2.171	2.164
0.998	0.998000	2.564	2.186	2.178	2.171	2.164
0.999	0.999000	2.564	2.186	2.178	2.171	2.164
1	1.000000	2.564	2.186	2.178	2.171	2.164

Table 31. Results of computed S-wave velocities versus saturation in Alberta Tight Gas Sand at different coupling factor values.

6.4.1.1.4 Interpreting shear-wave velocity models

The measured shear-wave velocity was higher than that of theoretical models because the drainage technique in establishing the saturation produced a non-uniform gas distribution. The shear-wave velocity decreased at low-water saturation, and then increased with increasing water saturation. The low porosity and permeability in tight gas sand with the drying technique explains why the shear velocity changed randomly.
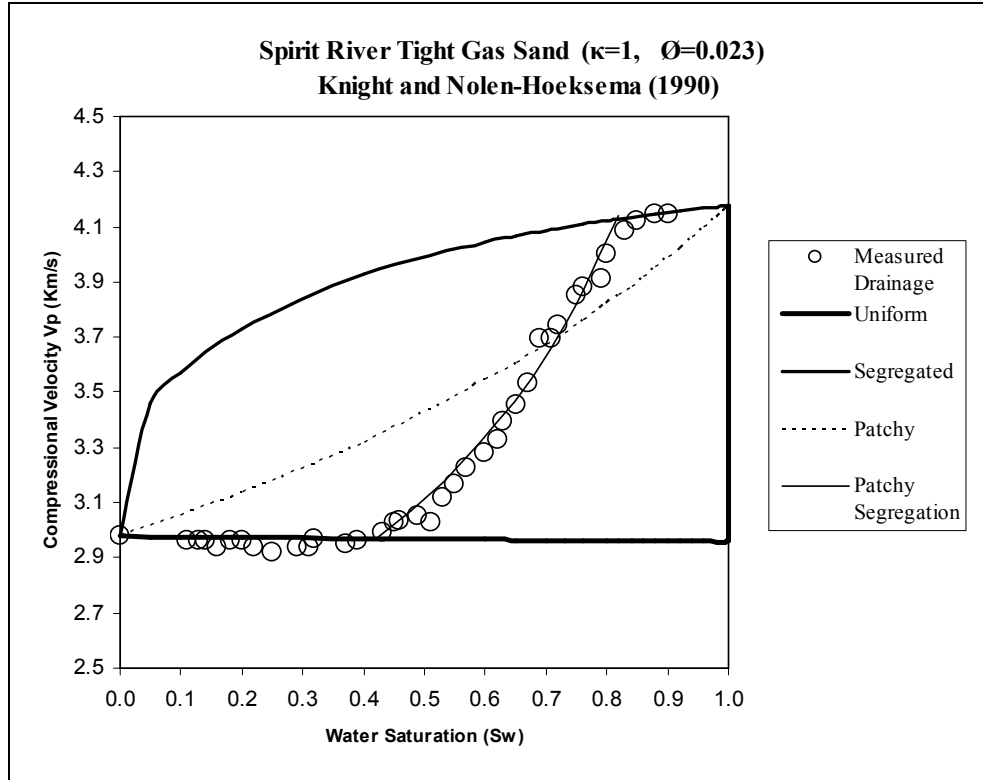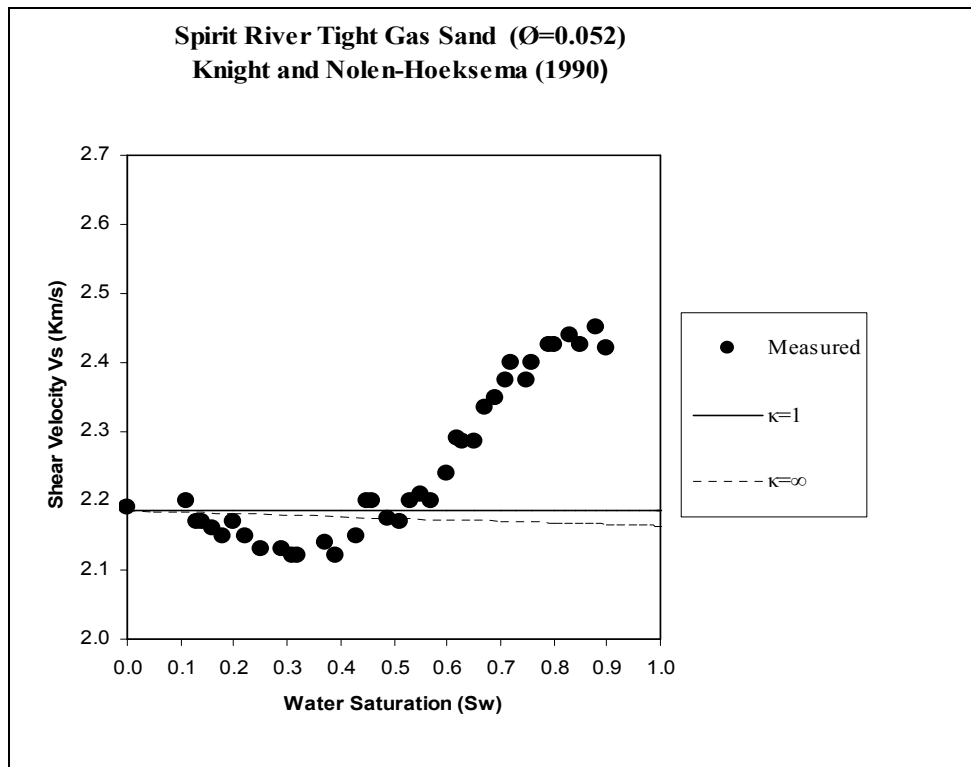
Figure (32): Curve fit of S-wave velocity in Alberta Tight Gas Sand as a function of water saturation from Knight and Nolen-Hoeksema (1990 at a coupling factor of (κ =1 and ∞). Solid circles are saturations established using a flow technique.

6.4.2 Sierra white granite

Murphy (1985) measured both the compressional and shear-wave velocities in Sierra white granite versus water saturation at a frequency of 200 kHz. The saturation was established using the drainage technique without any applied pressure. The ultrasonic velocity values of P-wave and S-wave versus water saturation are listed in Table (32). The sample porosity was very low about 0.008.

Average water saturation (S_w)	Compressional wave velocity V_P (km/s)	Shear wave velocity V_S (km/s)
0	4.350	2.740
0.11	4.470	2.740
0.22	4.520	2.760
0.33	4.610	2.760
0.36	4.710	2.830
0.4	4.730	2.820
0.45	4.900	2.850
0.56	4.940	2.850
0.68	5.060	2.880
0.78	5.430	2.910
0.86	5.520	2.970
1	5.560	2.980

Table 32. Measured compressional and shear wave velocity values versus saturation in Sierra white granite from Murphy (1985).Data taken from Gist (1994).

6.4.2.1 Modeling and interpreting measured and computed ultrasonic velocity models

6.4.2.1.1 Modeling the compressional wave velocity (P-wave)

The dynamic shear modulus (μ) was calculated from the measured shear velocity at full-gas saturation by Equation (50). The input and output parameters are listed in Table 33. The dynamic shear modulus (μ) did not change with the mass coupling factor (κ), because the porosity was very low. As the shear modulus was determined, the calculation of the effective bulk moduli (K_{sat}) began. From Equation (48), the input parameters were calculated starting with the frame compressibility (C_b) which was computed from the measured compressional and shear velocities by Equation (49). The

rock bulk density increased with water saturation since the density of water is higher than that of gas.

Input at $S_w = 0$					Output
ρ_f (g/cm³)	ρ_b (g/cm³)	V^2_s (km/s)	Ø	κ	μ (Gpa)
0.000088	2.629	4.796	0.008	1	19.74
0.000088	2.629	4.796	0.008	1.5	19.74
0.000088	2.629	4.796	0.008	2	19.74
0.000088	2.629	4.796	0.008	2.5	19.74
0.000088	2.629	4.796	0.008	3	19.74
0.000088	2.629	4.796	0.008	11	19.74
0.000088	2.629	4.796	0.008	∞	19.74

Table 33. Calculations of dynamic shear modulus at different values of mass coupling factor in Sierra White Granite at full gas saturation from Murphy (1985).

Some input parameters are listed in Table 34. The air compressibility was very high under no applied pressure.

ρ_w (g/cm³)	ρ_g (g/cm³)	$Ø_T$	C_b (Gpa⁻¹)	C_s (Gpa⁻¹)	$\beta = C_s/C_b$	$(1-\beta)$
1.0	0.000088	0.008	0.16	0.043	0.39	0.61

Table 34. Sierra white granite parameters used to calculate the effective bulk moduli.

The calculations of the three effective bulk moduli are listed in Table (35).

S_w	Reuss K_{sat} (Gpa)	Voigt K_{sat} (Gpa)	Patchy K_{sat} (Gpa)
0	6.279	6.279	6.279
0.05	6.250	14.142	6.847
0.1	6.250	16.061	7.445
0.2	6.250	19.042	8.740
0.4	6.250	22.958	11.813
0.6	6.250	25.416	15.758
0.65	6.250	25.894	16.925
0.7	6.250	26.331	18.182
0.73	6.250	26.576	18.983
0.76	6.250	26.809	19.822
0.8	6.250	27.103	21.006
0.82	6.250	27.243	21.628
0.84	6.250	27.378	22.271
0.86	6.250	27.510	22.936
0.88	6.250	27.638	23.625
0.9	6.250	27.762	24.339
0.92	6.250	27.883	25.079
0.94	6.251	28.000	25.847
0.96	6.251	28.114	26.644
0.98	6.252	28.224	27.471
0.99	6.253	28.279	27.897
0.992	6.254	28.289	27.984
0.994	6.255	28.300	28.070
0.996	6.258	28.311	28.157
0.998	6.265	28.321	28.244
0.999	6.281	28.327	28.288
1	28.332	28.332	28.332

Table 35. Results of calculated effective bulk moduli of uniform, segregated, and patchy saturation models in Sierra white granite at $\kappa=1$ and connected-to-total porosity ratio of one, from Murphy (1985).

Then the P-wave velocities of the three models were calculated from Equation (51), and the compressional wave velocity results of the three different distribution models are listed in Table 36.

S_w	ρ_f (g/cm³)	ρ_b (g/cm³)	$\mu = 12$ (Gpa)		
			Reuss V_P (km/s)	Voigt V_P (km/s)	Patchy V_P (km/s)
0	0.000088	2.629	4.343	4.343	4.344
0.05	0.050084	2.629	4.342	4.886	4.386
0.1	0.100079	2.630	4.342	5.056	4.430
0.2	0.200070	2.630	4.341	5.244	4.523
0.4	0.400053	2.632	4.341	5.410	4.726
0.6	0.600035	2.634	4.340	5.486	4.960
0.65	0.650031	2.634	4.340	5.498	5.024
0.7	0.700026	2.634	4.340	5.510	5.091
0.73	0.730024	2.635	4.339	5.516	5.132
0.76	0.760021	2.635	4.339	5.522	5.175
0.8	0.800018	2.635	4.339	5.529	5.233
0.82	0.820016	2.635	4.339	5.532	5.262
0.84	0.840014	2.636	4.339	5.535	5.293
0.86	0.860012	2.636	4.339	5.538	5.324
0.88	0.880011	2.636	4.339	5.541	5.355
0.9	0.900009	2.636	4.339	5.544	5.387
0.92	0.920007	2.636	4.339	5.546	5.420
0.94	0.940005	2.636	4.339	5.549	5.453
0.96	0.960004	2.636	4.339	5.551	5.487
0.98	0.980002	2.637	4.339	5.554	5.521
0.99	0.990001	2.637	4.339	5.555	5.538
0.992	0.992001	2.637	4.339	5.555	5.542
0.994	0.994001	2.637	4.339	5.555	5.545
0.996	0.996000	2.637	4.340	5.556	5.549
0.998	0.998000	2.637	4.341	5.556	5.552
0.999	0.999000	2.637	4.343	5.556	5.554
1	1.000000	2.637	5.556	5.556	5.556

Table 36. Results of computed P-wave velocities versus saturation of the uniform, segregated, and simple patchy models in Sierra White Granite.

Figure (33) shows Sierra white granite velocity curves versus water saturation for both measured and computed compressional wave velocities at a coupling factor of one ($\kappa = 1$), and connected-to-total porosity ratio of one.
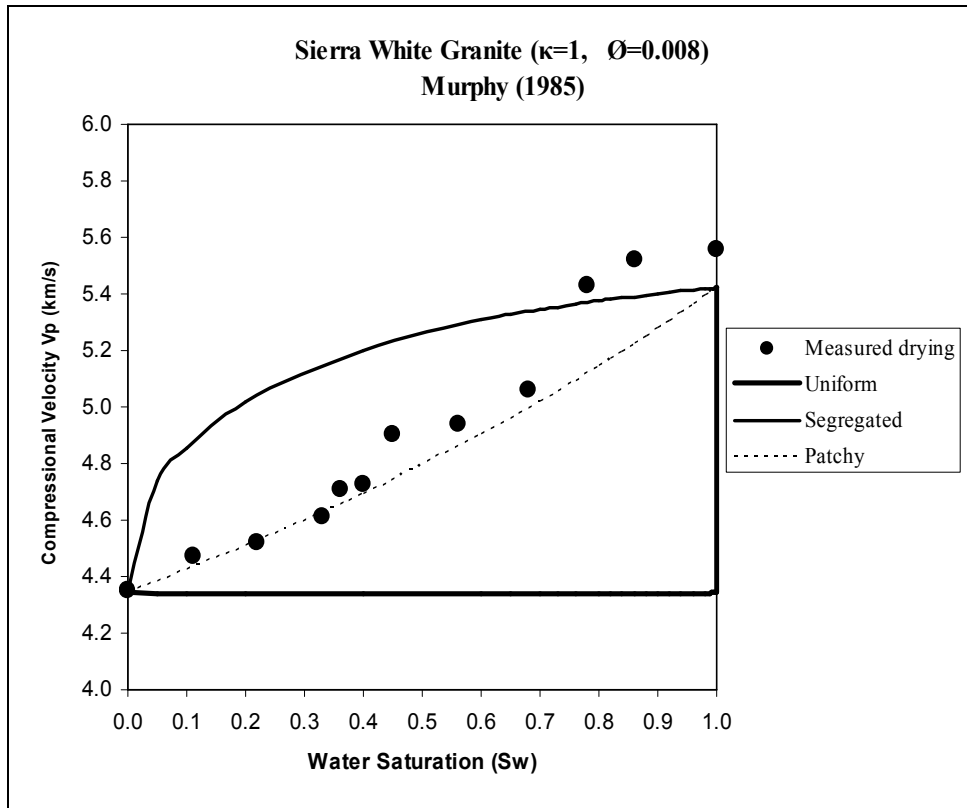
Figure (33): Results of P-wave velocity models in Sierra white granite as a function of water saturation from Murphy (1985) at coupling factor of one (κ=1), porosity of 0.008.

Because the porosity is very low, some errors in separating the total porosity could have given wrong results at the ending point. The ending point did not match the theoretical models. The ending point was able to be matched if the porosity decreased to a value of 0.035. We consider there was an error in measuring the porosity through the laboratory experiments. The results of reducing the porosity are shown in Figure 34.
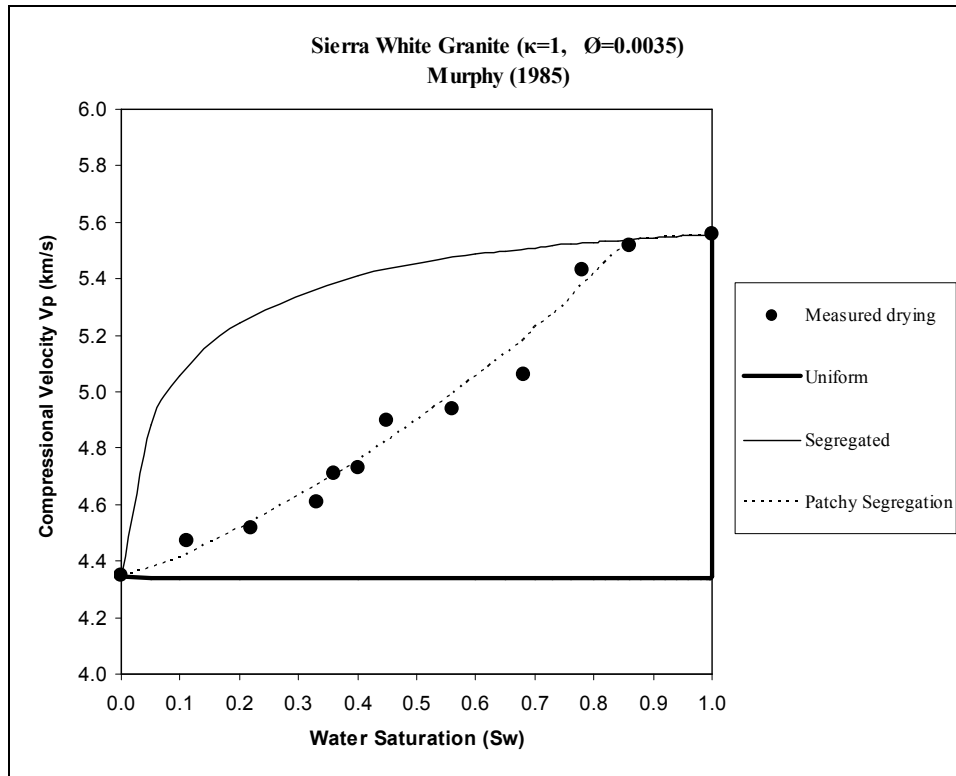
Figure (34): Curve fit of P-wave velocity models in Sierra white granite as a function of water saturation from Murphy (1985). Curve fit parameters include coupling factor of one ($\kappa =1$), total connected porosity = 0.0035, and patchy segregation model from S_w = 0% to S_w= 86 %. Solid circles are saturations established using the drying technique

The patchy segregation model calculations are listed below Table 37.

S_w	K_{uni}	K_{seg}	K_{uni}+4/3μ	K_{seg}+4/3μ	4/3μ	K_{eff}	ρ_b	Vp
0	23.28	23.28	49.595	49.595	26.315	23.280	2.629	4.343
0.116	23.25	41.074	49.565	67.315	26.315	24.814	2.633	5.047
0.24	23.25	47.176	49.565	73.491	26.315	27.309	2.633	5.376
0.35	23.25	49.513	49.565	75.828	26.315	30.087	2.633	5.429
0.465	23.25	51.23	49.565	77.543	26.315	33.242	2.633	5.482
0.58	23.25	52.599	49.565	78.914	26.315	36.882	2.633	5.538
0.79	23.251	53.42	49.566	79.732	26.315	44.381	2.633	5.538
0.82	23.251	53.583	49.566	79.898	26.315	45.655	2.633	5.538
0.87	23.251	53.935	49.566	80.250	26.315	47.957	2.633	5.538
0.91	23.251	54.144	49.566	80.459	26.315	49.870	2.633	5.538
1	23.251	54.428	49.566	80.743	26.315	54.428	2.633	5.538

Table 37. Calculations of the patchy segregation model in Sierra white granite.

6.4.2.1.2 Interpreting compressional wave velocity models

Most measured P-wave velocity values fit the theoretical model of the patchy segregation model. At a high water saturation of S_w >86%, the measured value fits the fully segregated model. It is obvious that the very low porosity and permeability in the Sierra white granite sample led to a heterogeneous fluid distribution. The measured data did not fit the uniform model at all; uniform distribution did not exist. The transitional zone dominated most of the measured values. The measured compressional velocity increased linearly with increasing water saturation. The heterogeneity in fluid distribution increased with increasing water saturation. The lower the porosity and permeability of the rock, the faster the segregation of fluid distribution occurred.

6.4.2.1.3 Modeling the shear-wave velocities (S-wave)

The calculated shear-wave velocity versus water saturation were listed at different values of mass coupling factors (κ =1, and ∞), and Table (38) shows the results. The data were measured during the drainage cycle. The measured and calculated shear-wave velocities versus water saturation were modeled and appear in Figure (35).

S_w	ρ_f (g/cm³)	ρ_b (g/cm³)	$\kappa = 1$ $\mu=19.736$ (Gpa)	$\kappa = 1.5$ $\mu=19.736$ (Gpa)	$\kappa = 3$ $\mu= 19.736$ (Gpa)	$\kappa = \infty$ $\mu= 19.736$ (Gpa)
			V_S (km/s)	V_S (km/s)	V_S (km/s)	V_S (km/s)
0	0.000088	2.629	2.740	2.740	2.740	2.740
0.05	0.050084	2.629	2.740	2.740	2.740	2.740
0.1	0.100079	2.630	2.740	2.740	2.740	2.740
0.2	0.200070	2.630	2.740	2.740	2.739	2.739
0.4	0.400053	2.632	2.740	2.739	2.739	2.738
0.6	0.600035	2.634	2.740	2.739	2.738	2.738
0.65	0.650031	2.634	2.740	2.739	2.738	2.737
0.7	0.700026	2.634	2.740	2.739	2.738	2.737
0.73	0.730024	2.635	2.740	2.739	2.738	2.737
0.76	0.760021	2.635	2.740	2.739	2.738	2.737
0.8	0.800018	2.635	2.740	2.739	2.738	2.737
0.82	0.820016	2.635	2.740	2.739	2.738	2.737
0.84	0.840014	2.636	2.740	2.739	2.738	2.737
0.86	0.860012	2.636	2.740	2.739	2.738	2.736
0.88	0.880011	2.636	2.740	2.739	2.738	2.736
0.9	0.900009	2.636	2.740	2.739	2.738	2.736
0.92	0.920007	2.636	2.740	2.739	2.737	2.736
0.94	0.940005	2.636	2.740	2.739	2.737	2.736
0.96	0.960004	2.636	2.740	2.739	2.737	2.736
0.98	0.980002	2.637	2.740	2.739	2.737	2.736
0.99	0.990001	2.637	2.740	2.739	2.737	2.736
0.992	0.992001	2.637	2.740	2.739	2.737	2.736
0.994	0.994001	2.637	2.740	2.739	2.737	2.736
0.996	0.996000	2.637	2.740	2.739	2.737	2.736
0.998	0.998000	2.637	2.740	2.739	2.737	2.736
0.999	0.999000	2.637	2.740	2.739	2.737	2.736
1	1.000000	2.637	2.740	2.739	2.737	2.736

Table 38. Results of computed S-wave velocities versus saturation in Sierra white granite different coupling factor values.
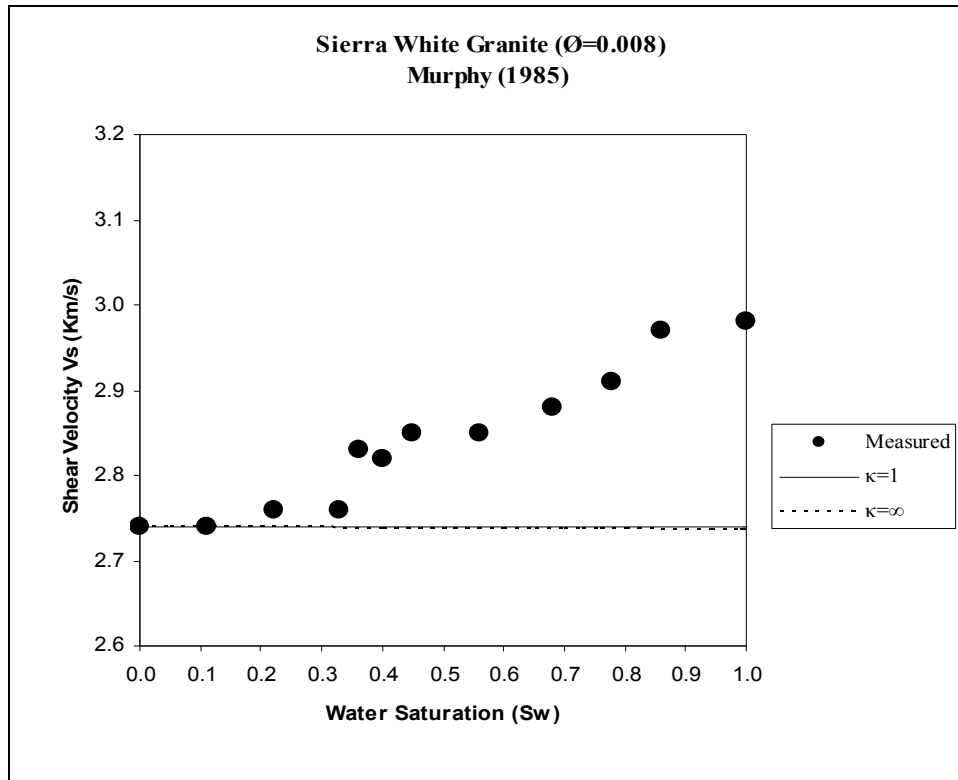
Figure (35): Curve fit of S-wave velocity in Sierra white granite as a function of water saturation from Murphy (1985) at a coupling factor of (κ=1 and ∞).Solid circles are saturations established using the drying technique.

6.4.2.1.4. Interpreting shear-wave velocity models

The measured shear-wave velocity was higher than that of the theoretical models for most saturation ranges. At low-water saturation the velocity was in good agreement with the theoretical models. Because the porosity and permeability were very low, there was no big difference between the theoretical models at different coupling factors. The drying technique exhibited higher shear velocities with increasing water saturation.

Chapter 7   CONCLUSIONS AND DISCUSSION

Laboratory measurements of ultrasonic compressional and shear-wave velocities can match the Biot theory by using the separation of the total porosity into acoustically connected and disconnected. The ratio of connected to disconnected porosity is a simple parameter that allows the ending points of the saturation curves to be matched.

Using different values of the mass coupling factor in the calculation of the ultrasonic velocities helped in matching the values correctly. Changing the mass coupling factor helped in better fitting the data. The coupling factor is assumed to be one at ultrasonic velocities. Varying the value of the mass coupling factor could balance for the error in the assumed value.

Using the patchy segregation model explained the transitional behavior of the measured compressional velocities. The patchy segregation model is controlled by the size and distribution of the fluid patches. The size and geometry of the pores are very important properties in controlling the shape of the velocity-saturation curves. The theoretical models of the uniform, patchy segregation and segregated distribution explained the measured data of all type of rocks.

With our methods presented here, no correction is required for the attenuation and dispersion mechanism (Biot and squirt) that could occur at high water saturation, because the porosity is separated into acoustically connected to disconnected portions.

Using the effective solid compressibility and different coupling factor values compensated for the theoretical errors in correcting for dispersion, especially in high porosity and permeability rocks.

Sonic logs and laboratory velocity measurements exhibit large dispersion effects that should be corrected in order to have accurate interpretations. Sonic log velocities can be affected by the non-uniform distribution of the gas fluid at low gas saturation. Non-uniform partially gas saturation occurs in an invaded area around the borehole. Invasion corrections need accurate estimation of the water saturation and porosity. The fluid distribution in the reservoir is not known, but if we know the velocity then we can predict what type of saturation the reservoir has. This situation is the same when the reservoir is in production; the fluid saturation and distribution changes with time and the reservoir does not have a uniform distribution, but the saturation probably will be a patchy segregation of mixed phases of uniform and segregated.

Measured shear-wave velocities were used in the calculation of the effective bulk moduli, an error in measuring the shear-wave velocities will significantly affect the calculations. Compressional wave velocities of the sonic log can be predicted using the results of this research, if accurate shear-wave velocities are predicted at the saturated zones.

8. References

Anthony L. Endres and Rosemary J. Knight., 1997, Incorporating pore geometry and fluid pressure communication into modeling the elastic behavior of porous rocks, Geophysics, 01731-3010.

Batzle, M., Han D., and Castagna, J. P., 1999, Fluids and frequency dependent seismic velocity of rocks: Expanded Abstract, 69th Annual Meeting, Society of Exploration Geophysicists, 5-8.

Batzle, M., and Wang, Z., 1992, Seismic properties of pore fluids: Geophysics, vol. 57, No. 11, 1396-1408.

Biot, M. A., 1956b, Theory of propagation of elastic waves in fluid-saturated porous solids. II. Higher frequency range: J. Acoust. Soc. Am., v.28,179–191.

Castagna, J. P., Batzle, M. L., and Kan, T. K., 1993, Rock physics; the link between rock properties and AVO response: *in* J. P. Castagna and M. M. Backus, Eds., Offset Dependent Reflectivity - Theory and Practice of AVO Analysis, Society of Exploration Geophysicists

Castagna, J., and Hooper, J., 2000, A simple method for fitting P-wave velocity versus saturation curves: 70th Ann. Internat. Mtg., Soc.Expl. Geophys. Expanded Abstracts, 1887–1890.

Domenico, S. N.. 1974. Effect of water saturation on seismic reflectivity of sand reservoirs encased in shale: Geophysics v.39. D. 759-769.

Domenico, S. N., 1976, Effect of brine-gas mixture on velocity in an unconsolidated sand reservoir: Geophysics, v. 41,882-894.

Domenico, S. N., 1977, Elastic properties of unconsolidated porous sand reservoirs: Geophysics, 42, 1339.

Dvorkin, J., and Nur, A., 1993, Dynamic poroelasticity: A unified model with the squirt and Biot mechanism: Geophysics, v. 58,524–533.

Endres, A. L., and Knight, R., 1991, The effects of pore scale fluid distribution on the physical properties of partially saturated tight sandstones: J. Appl. Phys., v.69,1091–1098.

Gardner, Cl. H. F., Gardner, L. W., and Gregory, A. R., 1974, Formation velocity and density-the diagnostic basis of stratigraphic traps: Geophysics, v.39, p. 770-780.

Gary Mavko and Diane Jizba, The relation between seismic P- and S- wave velocity dispersion in saturated rocks, Geophysics, v.59, no. 1 (January 1994); P. 87-92, 7.

Geertsma, J., and Smit, D. C., 1961, Some aspects of elastic wave propagation in fluid-saturated porous solids: Geophysics, v.26, p. 169-181.

Gregory, A. R., 1976, Fluid saturation effects on dynamic elastic properties of sedimentary rocks: Geophysics, v.41,895-92 1.

Gist, G. A., 1994 Interpreting laboratory velocity measurements in partially saturated gas-saturated rocks: Geophysics, v.59, 1100-1109

Hilterman, F. J., 2001, Seismic amplitude interpretation: Short Soc. Expl. Geophys. Distinguished Instructor Series 4.

James G. Berryman, Tutorial Origin of Gassmann's equations, Geophysics, v.64, No. 5 (September-October 1999); P. 1627–1629.

Knight, R., and Nolen-Hoeksema, R., 1990, A laboratory study of the dependence of elastic wave velocities on pore scale fluid distribution: Geophysics. Res. Lett, v.17,1529 532.

Mavko, G., and Mukerji, T., 1998, Bounds on low-frequency seismic velocities in partially saturated rocks, Geophysics, v.63, 918-924.

Mavko, G., Mukerji, T., and Dvorkin, J., 1998, The rock physics handbook—Tools for seismic analysis in porous media: Cambridge Univ. Press.

Murphy, W. F., Effects of microstructure and pore fluids on the acoustic properties of granular sedimentary materials: Ph.D. dissertation, Stanford University.

Murphy, W. F., Winkler, K.W., and Kleinberg, R. L., 1985, Acoustic relaxation in sedimentary rocks: Dependence on grain contacts and fluid saturation, Geophysics, v.51. No. 3 (March 1986); P. 757-766.

Smith, T.M., Sondergeld, C.H., and Rai, C.S., Gassmann fluid substitutions: A tutorial, Geophysics v.68, No.2 (March-April 2003); P.430-440

Wang, Z., 2001, Fundamentals of seismic rock physics: Geophysics, v.66,398–412.